

INFORMATION TO USERS

This manuscript has been reproduced from the microfilm master. UMI films the text directly from the original or copy submitted. Thus, some thesis and dissertation copies are in typewriter face, while others may be from any type of computer printer.

The quality of this reproduction is dependent upon the quality of the copy submitted. Broken or indistinct print, colored or poor quality illustrations and photographs, print bleedthrough, substandard margins, and improper alignment can adversely affect reproduction.

In the unlikely event that the author did not send UMI a complete manuscript and there are missing pages, these will be noted. Also, if unauthorized copyright material had to be removed, a note will indicate the deletion.

Oversize materials (e.g., maps, drawings, charts) are reproduced by sectioning the original, beginning at the upper left-hand corner and continuing from left to right in equal sections with small overlaps.

Photographs included in the original manuscript have been reproduced xerographically in this copy. Higher quality 6" x 9" black and white photographic prints are available for any photographs or illustrations appearing in this copy for an additional charge. Contact UMI directly to order.

ProQuest Information and Learning
300 North Zeeb Road, Ann Arbor, MI 48106-1346 USA
800-521-0600

UMI[®]

UNIVERSITY OF ALBERTA

LARGE DEFLECTIONS OF A MAGNETICALLY ACTUATED
MICROCANTILEVER WITH AN ON-CHIP PERMALLOY LAYER

BY



BING YU

A THESIS

SUBMITTED TO THE FACULTY OF GRADUATE STUDIES AND
RESEARCH

IN PARTIAL FULFILLMENT OF THE REQUIREMENT FOR THE DEGREE
OF

MASTER OF SCIENCE

DEPARTMENT OF ELECTRICAL AND COMPUTER ENGINEERING

EDMONTON, ALBERTA

FALL 2000



National Library
of Canada

Acquisitions and
Bibliographic Services

395 Wellington Street
Ottawa ON K1A 0N4
Canada

Bibliothèque nationale
du Canada

Acquisitions et
services bibliographiques

395, rue Wellington
Ottawa ON K1A 0N4
Canada

Your file Votre référence

Our file Notre référence

The author has granted a non-exclusive licence allowing the National Library of Canada to reproduce, loan, distribute or sell copies of this thesis in microform, paper or electronic formats.

The author retains ownership of the copyright in this thesis. Neither the thesis nor substantial extracts from it may be printed or otherwise reproduced without the author's permission.

L'auteur a accordé une licence non exclusive permettant à la Bibliothèque nationale du Canada de reproduire, prêter, distribuer ou vendre des copies de cette thèse sous la forme de microfiche/film, de reproduction sur papier ou sur format électronique.

L'auteur conserve la propriété du droit d'auteur qui protège cette thèse. Ni la thèse ni des extraits substantiels de celle-ci ne doivent être imprimés ou autrement reproduits sans son autorisation.

0-612-59909-4


Canada

UNIVERSITY OF ALBERTA
RELEASE FORM

NAME OF AUTHOR: **BING YU**
TITLE OF THESIS: **LARGE DEFLECTIONS OF A
MAGNETICALLY ACTUATED
MICROCANTILEVER WITH AN
ON-CHIP PERMALLOY LAYER**
DEGREE: **MASTER OF SCIENCE**
YEAR THIS DEGREE GRANTED: **2000**

PERMISSION IS HEREBY GRANTED TO THE UNIVERSITY OF ALBERTA
LIBRARY TO REPRODUCE SINGLE COPIES OF THIS THESIS AND TO
LEND OR SELL SUCH COPIES FOR PRIVATE, SCHOLARLY OR
SCIENTIFIC RESEARCH PURPOSES ONLY.

THE AUTHOR RESERVES ALL OTHER PUBLICATION RIGHTS, IN
ASSOCIATION WITH THE COPYRIGHT IN THE THESIS, AND EXCEPT
AS HEREIN BEFORE PROVIDED NEITHER THE THESIS NOR ANY
SUBSTANTIAL PORTION THEREOF MAY BE PRINTED OR OTHERWISE
REPRODUCED IN ANY MATERIAL FORM WHATEVER WITHOUT THE
AUTHOR'S WRITTEN PERMISSION.

(SIGNED) 

BING YU
7 - 10304 - 107 AVE.
EDMONTON, AB
CANADA

DATE: *July 28, 2000*

Abstract

Efforts have been made to integrate a magnetic material, Permalloy, into micromachined devices. Magnetic characteristics of the Permalloy deposited by electroplating technique were measured, with the saturation magnetization of 0.56 Tesla along the material's longest axis, coercive force of 3 Gauss and remnant magnetization of 0.22 Tesla. An acceptable thickness and composition uniformity of the material has been obtained. Little internal stress was observed in the microstructure during the deposition of the magnetic material.

The microstructure was designed as a rectangular platform supported by two SiO_2 cantilever arms at the far end. On the top of the platform a $270\text{ }\mu\text{m} \times 200\text{ }\mu\text{m} \times 5\text{ }\mu\text{m}$ Permalloy film was deposited by electroplating. Actuation of the structure is based on the magnetic torque produced by the interaction between the on-chip Permalloy and an external magnetic field. The deflection of the central platform was measured in both static and dynamic cases. A static deflection of 60° has been achieved with a DC magnetic field of 130 Gauss, which matches the theoretical prediction well. In dynamic measurement, we found that a DC offset field is necessary to actuate the device. Two resonant frequencies have been measured, at 380 Hz and 590 Hz. The deflections at the resonant frequencies are 52° with 3.6 Gauss AC field superimposed on a 16 Gauss DC field and 17° with 3.6 Gauss AC field superimposed on a 2 Gauss DC magnetic field respectively.

University of Alberta

Faculty of Graduate Studies and Research

The undersigned certify that they have read, and recommend to the Faculty of Graduate Studies and Research for acceptance, a thesis entitled **LARGE DEFLECTIONS OF A MAGNETICALLY ACTUATED MICROCANTILEVER WITH AN ON-CHIP PERMALLOY LAYER** submitted by **Bing Yu** in partial fulfillment of the requirements for the degree of Master of Science.



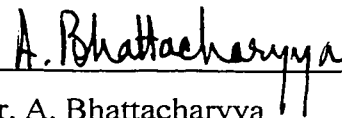
Dr. A. M. Robinson, supervisor



Dr. W. Allegretto, supervisor



Dr. F. E. Vermeulen



Dr. A. Bhattacharyya

Date: July 27, 2000

Acknowledgements

I would like to express my sincere gratitude to my supervisors Dr. A. M. Robinson and Dr. W. Allegretto, for their patience, encouragement and guidance throughout this research work. Special appreciation should be extended to Dr. R. P. W. Lawson, Dr. Tianshen Zhou, and Dr. F. Vermulen for their enlightening discussion in various areas. Dr. N. Tait at Alberta Microelectronic Corporation (AMC) has provided invaluable help and support with the device processing, to which I am grateful.

I wish to acknowledge the processing support provided by AMC. Special thanks to G. Mckinnon, Y. Ning, K. Westra, Jim Broughton and Lianne Læster for their instructions and assistance with the facilities at AMC, as well as for their helpful suggestion and advice, and to Dr. J. Jung and Dr. F. Franck in the Department of Physics, University of Alberta, for help measuring sample magnetic material.

I am also grateful to D. Haley, A. Chan, K. Brown, D. Strembicke and Yuan Ma for their continuous support.

Finally, my heartfelt gratitude goes to my wife and family for their willing support and help, especially during difficult times. This thesis is dedicated to them.

Contents

1	Introduction	1
1.1	Actuation Technologies.....	1
1.2	Electroplating Process.....	4
1.3	Motivations and Thesis Overview.....	6
2	Magnetic Actuation of the Device	7
2.1	Magnetic Analysis	7
2.1.1	Magnetic Anisotropy	8
2.1.2	Magnetic Anisotropy Torque.....	16
2.2	Magnetic Torque.....	17
3	Fabrication	22
3.1	The Selection of the Magnetic Materials.....	22
3.2	The Electroplating of NiFe.....	24
3.3	The Electroplating of a Standard CMOS-Processed Device.....	34
3.4	The Fabrication of the Devices.....	36
4	Mechanical Analysis of the Device	43
4.1	The Structure of the device.....	43

4.2	Mechanical Analysis.....	44
4.2.1	Static Deflection.....	44
4.2.2	Dynamic Response.....	50
5	Experimental Results and Discussion	53
5.1	Experimental Equipment.....	53
5.1.1	Magnetic Field Source.....	53
5.1.2	Microscope.....	56
5.2	Experimental Set-up and Results.....	56
5.2.1	Static Deflection.....	57
5.2.2	Dynamic Response.....	59
6	Conclusions and Outlook	68

List of Tables

Table 2.1 Crystalline anisotropy constants at room temperature.....	9
Table 3.1 NiFe plating bath recipe.....	27
Table 4.1 Structure Dimensions in μm	43

List of Figures

1.1	Basic electroplating system.....	5
2.1	The general ellipsoid ($b > a > c$) used to calculate the shape coefficient N_a , N_b , and N_c	11
2.2	Shape coefficient of the general ellipsoid along the long axis.....	12
2.3	Shape coefficient of the general ellipsoid along the medium axis.....	13
2.4	Shape coefficient of the general ellipsoid along the short axis.....	13
2.5	Magnetization model of our device.....	15
2.6	A permanent magnetic material with α degree to an external magnetic field \vec{B}	19
2.7	Magnetization of a magnetic material under a magnetic field.....	19
2.8	Angle between the magnetization and the easy axis versus external magnetic field.....	21
3.1	Saturation magnetization versus percentage Nickel in Iron.....	23
3.2	Micrographs of $Ni_{80}Fe_{20}$ and $Ni_{50}Fe_{50}$ samples.....	24
3.3	Cross-section of the selective electroplate.....	25
3.4	Weight percentage of iron in nickel versus current density.....	29
3.5	Current density through the wafer.....	30
3.6	Thickness of the NiFe on the wafer.....	30
3.7	The fabrication process of the frame plating technique.....	33
3.8	Hysteresis curve of the plated NiFe alloy along the longest side.....	35

3.9	Hysteresis curve of the plated NiFe alloy along the shortest side.....	35
3.10	Top view of the CIC device.....	37
3.11	Cross-section and top view of the fabrication process flow.....	42
3.12	Undercut of silicon anisotropic etch.....	42
4.1	Top view of the structure.....	44
4.2	Hysteresis curve of the magnetic material along the longest axis.....	45
4.3	Side view of the deflected structure.....	46
4.4	Theoretic deflection angle versus magnetic field.....	49
4.5	The first resonant mode of the device.....	51
4.6	The second resonant mode of the device.....	52
4.7	The third resonant mode of the device.....	52
5.1	Configuration of the electromagnet.....	54
5.2	Generated magnetic field versus applied voltage.....	55
5.3	Magnetic field generated by electromagnet versus frequency.....	56
5.4	Simplified model for static deflection measurement.....	58
5.5	Comparison of the experimental and theoretic static deflection.....	58
5.6	A sketch of the torque versus time t	60
5.7	The set-up used for dynamic response measurement.....	62
5.8	Relative deflection angle versus frequency with a 0.6 V DC offset superimposed on a 2 V peak-to-peak sinusoidal voltage applied to the electromagnet.....	63
5.9	Relative deflection angle of the device at 3.6 Gauss AC magnetic field and 2 Gauss offset.....	64

5.10	Comparison of the relative deflection angles at 16 Gauss and 2 Gauss DC magnetic fields with 3.6 Gauss AC magnetic field.....	66
5.11	Comparison of deflection angles of 3.6 Gauss and 3 Gauss AC magnetic field with 16 Gauss DC offset.....	67

Chapter 1

INTRODUCTION

1.1 Actuation Technologies

The term MEMS (Micro-Electro-Mechanical System) refers to a broad family of micromachined sensors, actuators and systems. MEMS devices can be used either to sense physical or chemical measurands, or to achieve a desired movement or displacement.

Actuation of a micromachined device normally involves an energy conversion from an electrical or magnetic form into a quantity of another form such as mechanical. As an example, a micromachined microphone that is normally constructed with a thin movable membrane and a fixed substrate receives an electrical signal and outputs a mechanical signal, the vibration of the thin movable membrane, to produce sound. The most frequently used actuation mechanisms in MEMS include thermal actuation, piezoelectric actuation, electrostatic actuation, and magnetic actuation.

Thermal actuation [1, 2, 3, 4] makes use of a heating element to produce a temperature distribution through a microstructure. Due to thermal expansion of the structural material, this temperature distribution induces a strain on the structure. Thermal actuation has the advantage of easy operation; however, the thermal power produced by the heating element will produce a relatively slow response and an elevated temperature, which will degrade the performance of the device because most of the material parameters are temperature dependent.

Piezoelectric actuation [5, 6] involves the deposition of a piezoelectric material on a flexural structure. The piezoelectric material has the characteristic of producing a mechanical stress when a voltage is applied to it. The deposition of the piezoelectric material on a semiconductor substrate usually brings a compressive stress through the structure, resulting in an initial strain or bending of the structure.

More recently, electrostatic and magnetic actuation has appealed to many research groups. Electrostatic actuation [7, 8, 9] uses the electrostatic force generated when a voltage is applied between two adjacent electrodes. Normally, one or both electrodes are fabricated on movable structures. Electrostatic actuation is the most popular of all the actuation mechanisms since the fabrication techniques used to create electrostatic-actuated microstructures are the same as those used to construct integrated circuits (ICs). Electrostatic systems have already been successfully integrated with electronic circuits in a single batch-fabrication process to form complete micro-electro-mechanical systems [10].

Magnetic actuation makes use of magnetic force generated by the interaction between magnetic elements. Magnetic elements could include a magnetic field, ferromagnetic materials, or simply a coil with a current flowing in it. Magnetic actuation based on the interaction between a magnetic field and an on-chip current-carrying coil was first investigated by Shen [11, 12, 13]. In his work, a deflection-enhanced, cantilever-in-cantilever structure (CIC) was designed, and the device was fabricated by a standard CMOS process. The device was driven by an external magnetic field. A drawback of his work is that a large magnetic field is needed to achieve large deflection. Another magnetic actuation approach is based on the interaction between a magnetic field and a magnetic material [14, 15]. The magnetic material is deposited on a microstructure by electroplating or sputtering. The magnetic field could be produced by either an on-chip or an off-chip magnet.

By comparing the force generated by electrostatic and magnetic actuation, we can determine how well these two actuation mechanisms fit specific applications.

The force F that an actuator can generate is equal to the negative spatial derivative of the energy W stored between the armature and the stator ($\vec{F} = -\nabla \bar{W}$).

For a parallel-plate electrode system, the electrostatic energy density w_e is

$$w_e = \frac{\epsilon_o E^2}{2} \quad (1.1)$$

where ϵ_o is permittivity of free space.

Similarly, the magnetic energy density w_m stored in the air gap between the magnetic pole tips is

$$w_m = \frac{B^2}{2\mu_o} \quad (1.2)$$

where μ_o is permeability of free space.

The ratio of the magnetic to electrostatic energy densities is

$$\frac{w_m}{w_e} = \frac{B^2}{\mu_o \epsilon_o E^2} \quad (1.3)$$

If the fringing electrical field is ignored, we have $E = \frac{V}{d}$, where d is the distance between two electrodes. Assuming the magnetic material is saturated, and the saturated magnetization of the material is M_s , then B can be replaced by M_s .

Equation (1.3) becomes

$$\frac{w_m}{w_e} = \frac{M_s^2}{\mu_o \epsilon_o V^2} d^2 = \frac{c^2 M_s^2}{V^2} d^2 \quad (1.4)$$

where c is the speed of the light.

On a macroscopic scale, assuming d is in the range of 1 mm, the maximum electric field is $\sim 3 \text{ V} / \mu\text{m}$, and if a saturated magnetic material has a maximum flux density of 0.6 Tesla, then the above ratio is 3.6×10^3 . This result shows that magnetic actuation is more desirable for devices requiring large force or displacement.

1.2 Electroplating Process

In the last ten years, the success in the integration of micromachined devices and functional materials has prompted many research groups to investigate the performance, characterization and optimization of microstructures actuated by on-chip magnetic materials. Extensive applications based on electroplating magnetic materials on microstructures have been developed in magnetic printing heads, micro-electro-magnets, and magnetically actuated micromachined devices [16, 17, 18]. Although other processes such as sputtering can also deposit magnetic material, electroplating magnetic material has the advantage of producing thick films, which may be up to hundreds of microns thick.

A simple electroplating system, shown in Figure 1.1, includes two electrodes, a current source and a plating bath. A noble metal electrode is

normally chosen as the anode; the metal to be plated acts as the cathode; the plating bath contains the metal ions of those metals intended to be deposited on the cathode.

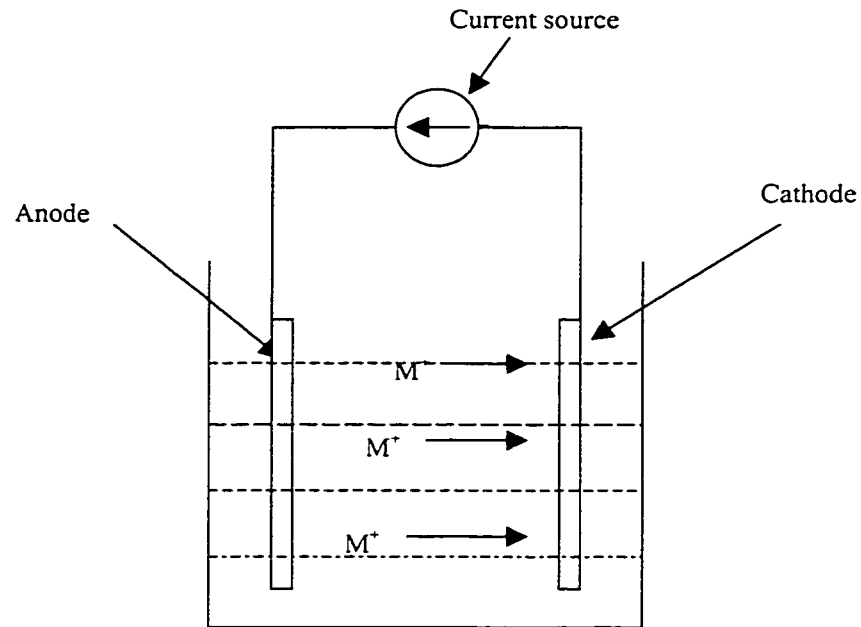


Figure 1.1 Basic Electroplating System

During electroplating, the current source provides current from the anode to the cathode. An electrical field is produced in the plating bath from the anode to the cathode, and drives metal ions in the vicinity of the cathode to the cathode. The metal ions capture electrons at the cathode and deposit the metal according to the equation:



1.3 Motivations and Thesis Overview

Magnetically actuated micromachined devices have become a simple and yet powerful approach especially applicable for applications requiring large force or displacement. Although microstructures actuated by on-chip Permalloy and an external magnetic field have been demonstrated by some research groups [14, 15, 19], it is still at a preliminary development stage. Most of the devices developed using this technology were fabricated by surface micromachining technology, and were studied under static conditions only. Performance improvement and fabrication process optimization of those devices would be the next and very critical step towards the commercialization of the technology.

In this thesis, we establish an inexpensive batch fabrication process to integrate a magnetic material, a NiFe alloy, onto a micromachined microstructure. The fabrication process has a minimum number of processing steps, and the electroplating process used to deposit the magnetic material is optimized to produce a stress-free material, which is critical to improve the performance of the microstructure.

Besides observing the static response, we also investigated the dynamic response of the device, and established an effective method of actuation.

This thesis consists of six chapters. The first chapter has briefly discussed the background and motivation for this research work. The second chapter analyses the magnetic characteristics of the magnetic material used in our device, and discusses the magnetic actuation of a prototype device under an external magnetic field. The next chapter describes the electroplating technology and the fabrication process of the device, while the fourth chapter analyzes the mechanical response of the device actuated by an external magnetic field. The fifth chapter presents the experimental results and compares them with the theoretical predictions. The last chapter concludes this thesis.

Chapter 2

MAGNETIC ACTUATION OF THE DEVICE

This chapter discusses the magnetic torque that can be generated between micro-magnetic elements and an external magnetic field. Some basic knowledge of the magnetic properties of Permalloy is introduced in Section 2.1. The magnetic torque generated on microstructures is discussed in Section 2.2.

2.1 Magnetic Analysis

We know that an atom can be regarded as a central positively charged nucleus surrounded by electrons. Electrons not only move around the nucleus in definite orbits but also spin about their own axes. Some electrons spin in one direction and some in the opposite direction. If the magnetization produced by the spin of the electrons is completely cancelled out, the material is non-magnetic. If the magnetization produced by the spin of the electrons is unbalanced, the material shows magnetic characteristics.

The magnetic behavior of various kinds of materials can be divided into three classifications: (1) diamagnetism, (2) paramagnetism, and (3) ferromagnetism. For diamagnetic or paramagnetic materials, if they are put in a magnetic field, the resultant magnetization in value is slightly less than or larger than the applied magnetic field. But for ferromagnetic materials, the resultant

magnetization can be thousands of times larger than the external magnetic field. This makes ferromagnetic materials very useful in the electrical industry.

Ferromagnetic materials in turn may be divided into two classes, those which retain a considerable amount of their magnetic energy after the magnetizing field has been removed, and those which lose most of their magnetism when the applied field is taken away. These two classes are known as “hard” and “soft” magnetic materials. The magnetization vector of a “hard” magnetic material, for example a permanent magnetic material, does not move or rotate. However, for “soft” magnetic materials, the magnetization vector can rotate away from its equilibrium position known as the “easy axis”. The degree to which the magnetization vector rotates away from the easy axis is determined by the magnetic anisotropy energy, which is a function of the physical and geometrical properties of the material and is a minimum along the easy axis.

In this work, it is desired that the deflection of the microstructure be controlled only by an external magnetic field, so the magnetic material we chose to deposit on the microstructure, a platform, is a “soft” magnetic material, a NiFe alloy. Therefore, the magnetic analysis discussed in this section only pertains to soft magnetic materials.

2. 1. 1 Magnetic Anisotropy

Magnetic anisotropy of a magnetic material refers to the dependence of the internal energy on the direction of spontaneous magnetization. As the internal magnetization is parallel to material’s stable direction (easy axis), the anisotropy energy is minimized. However as the internal magnetization rotates away from its easy axis, the anisotropy energy increases with an increase in ϕ , the angle between the easy axis and the internal magnetization, and takes its maximum value at $\phi = 90^\circ$. It then decreases again to minimum at $\phi = 180^\circ$. Without an external magnetic field, the internal magnetic energy of a magnetic material tends to maintain its minimum value. The larger the internal anisotropy energy along a

certain direction, the larger the external field required to magnetize a material along this direction.

The anisotropy energy is mainly determined by the crystalline structure of the magnetic materials (crystalline anisotropy). The crystalline anisotropy energy density can be expressed by expanding it in a series of powers of $\sin^2\phi$ according to [20]:

$$E_a = K_{u1} \sin^2 \phi + K_{u2} \sin^4 \phi + \dots \quad (2.1)$$

where K_{u1} and K_{u2} are crystalline constants of the magnetic material, and ϕ is the angle that the magnetization vector rotates away from the easy axis.

Usually the first term is sufficient to express actual anisotropy energy. Values of K_{u1} and K_{u2} for typical soft magnetic materials are given in table 2.1.

Table 2.1 Crystalline anisotropy constants at room temperature [21]

Material	K_{u1}	K_{u2}
Nickel	$-5 \times 10^3 \text{ J/m}^3$	$-2 \times 10^3 \text{ J/m}^3$
Iron	$4.8 \times 10^4 \text{ J/m}^3$	$5 \times 10^4 \text{ J/m}^3$
Cobalt	$4.5 \times 10^5 \text{ J/m}^3$	$-1.5 \times 10^5 \text{ J/m}^3$

Anisotropy energy of a magnetic material can be produced by applying mechanical stress to the material (stress anisotropy), or by treating the material with heating or cooling in a magnetic field (induced anisotropy). The stress and induced anisotropy energies can be formulated as

$$E_{stress} = K_{stress} \sin^2 \phi \quad (2.2)$$

$$E_{induced} = K_{induced} \sin^2 \phi \quad (2.3)$$

where K_{stress} and K_{induced} are stress and induced anisotropy constants[21, 22].

Typically, a 1.0 GPa stress on a NiFe alloy can induce a value for K_{stress} of $4.5 \times 10^4 \text{ J/m}^3$ [22].

The shape of a magnetic material also contributes to its anisotropy energy (shape anisotropy). The shape anisotropy energy is formulated as

$$E_{\text{shape}} = K_{\text{shape}} \sin^2 \phi \quad (2.4)$$

where K_{shape} is the shape anisotropy coefficient of the material.

The total anisotropy energy of a magnetic material is then

$$\begin{aligned} E_{\text{total}} &= E_{\text{induced}} + E_{\text{stress}} + E_{\text{crystalline}} + E_{\text{shape}} \\ &= (K_{\text{induced}} + K_{\text{stress}} + K_{\text{crystalline}} + K_{\text{shape}}) \sin^2 \phi \\ &= K_{\text{total}} \sin^2 \phi \end{aligned} \quad (2.5)$$

Of all the magnetic anisotropy energies, the contribution due to the shape of the magnetic material is the easiest to control. Shape anisotropy attempts to align the easy axis with the longest axis of the material. This can be explained by the shape coefficients N_a , N_b , and N_c , which are determined by the shape of the magnetic material and are defined for an ellipsoid because the material in this shape can be magnetized uniformly [23].

An ellipsoid has three shape coefficients N_a , N_b , and N_c , which correspond to each axis of the ellipsoid (Figure 2.1). In the rationalized-mks system of units, the sum of all three shape coefficients is always unity [23]:

$$N_a + N_b + N_c = 1 \quad (2.6)$$

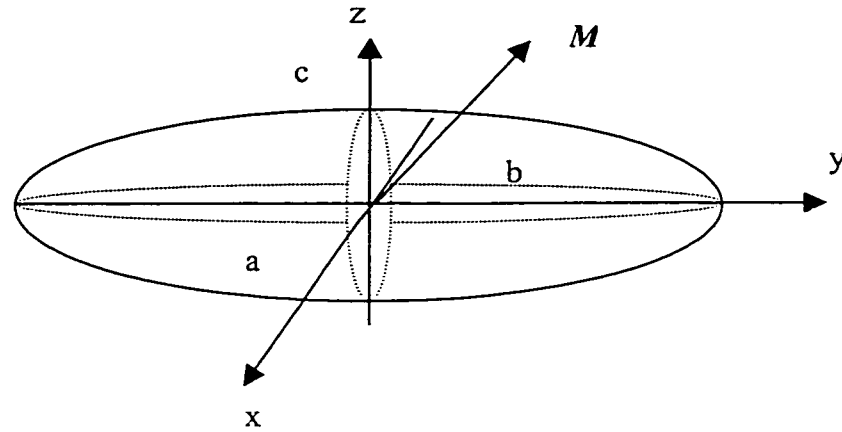


Figure 2.1 The general ellipsoid ($b > a > c$) used to calculate the shape coefficients N_a , N_b , N_c

N_a , N_b and N_c were first calculated by Osborn [23] in 1945, and expressed as

$$N_a = \frac{\cos \varphi \cos \delta}{\sin^3 \delta \sin^2 \alpha} [F(k, \delta) - E(k, \delta)]$$

$$N_b = \frac{\cos \varphi \cos \delta}{\sin^3 \delta \sin^2 \alpha \cos^2 \alpha} [E(k, \delta) - F(k, \delta) \cos^2 \alpha - \frac{\sin^2 \alpha \sin \delta \cos \delta}{\cos \varphi}]$$

$$N_c = \frac{\cos \varphi \cos \delta}{\sin^3 \delta \cos^2 \alpha} \left[\frac{\sin \delta \cos \varphi}{\cos \delta} - E(k, \delta) \right]$$

where $\cos \delta = \frac{c}{a}$

$$\cos \varphi = \frac{b}{a}$$

$$\sin \alpha = \frac{\sin \varphi}{\sin \delta} = k$$

$F(k, \delta)$ and $E(k, \delta)$ are the ellipsoidal integrals of the first and second kind, k is the modulus and δ is the amplitude of the ellipsoidal integrals. The semi-axes of the ellipsoid are a , b and c .

Judy wrote a computer program to calculate the shape coefficient [22]. The results plotted with logarithmic axes are shown in Figures 2.2 to 2.4.

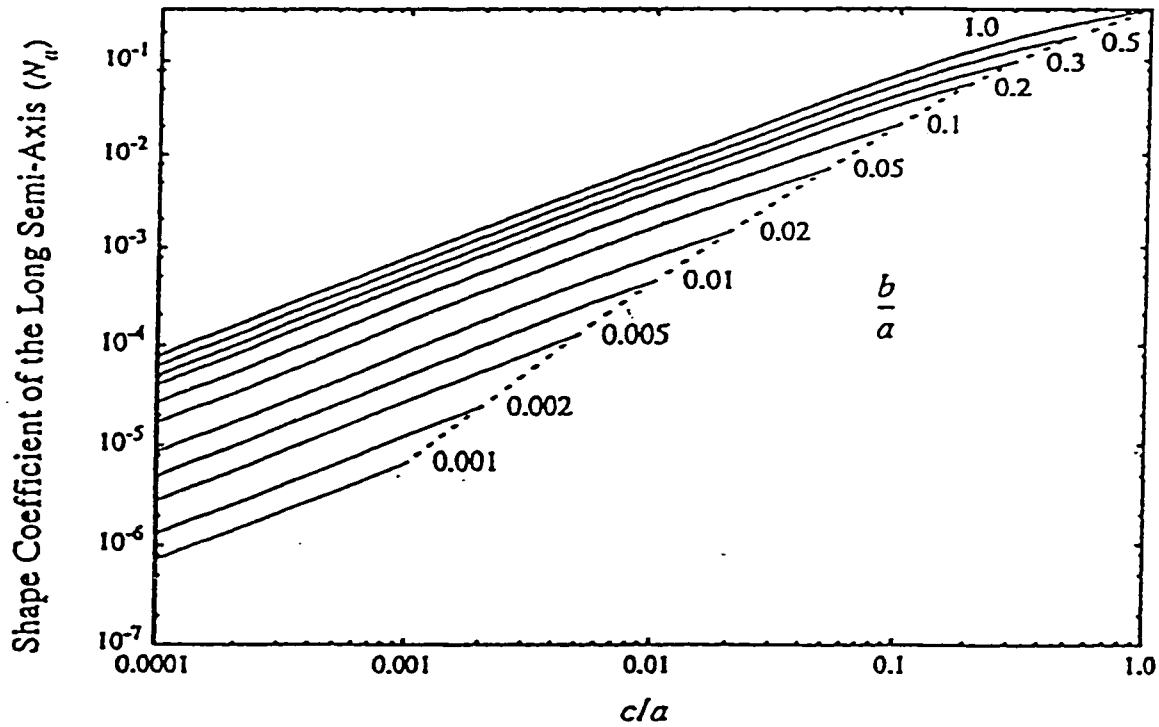


Figure 2.2 Shape coefficients of the general ellipsoid along the long axis N_u

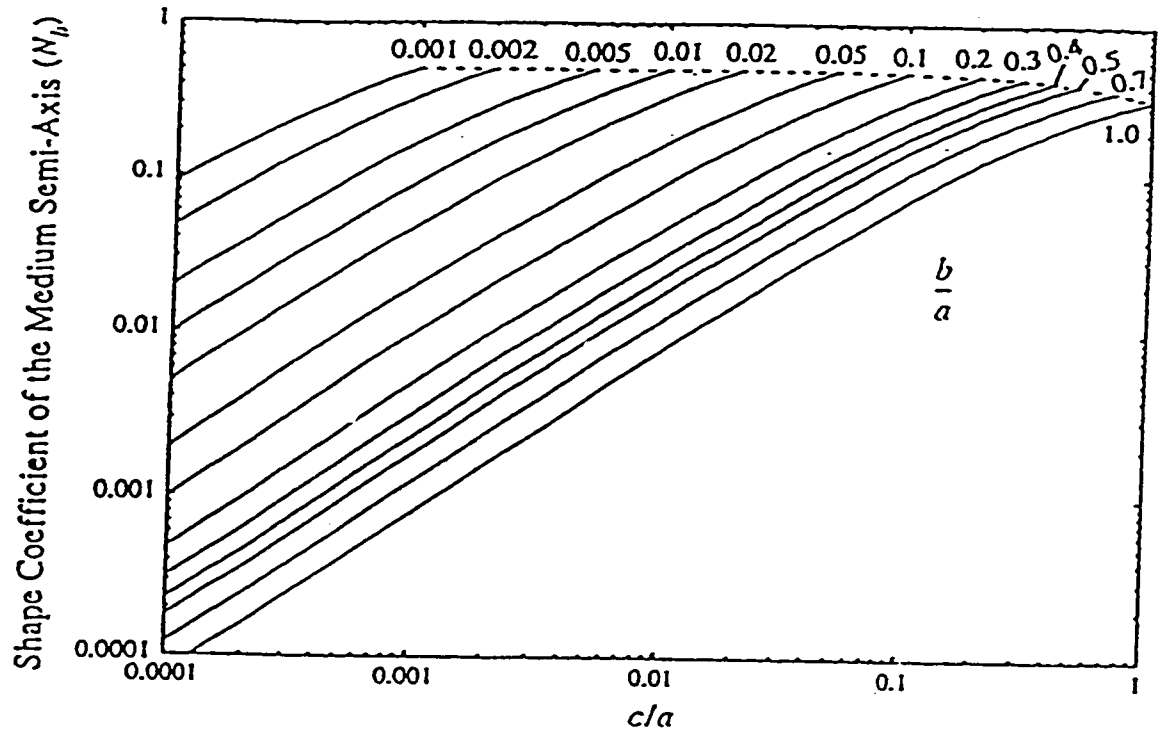


Figure 2.3 Shape coefficients of the general ellipsoid along the medium axis N_b

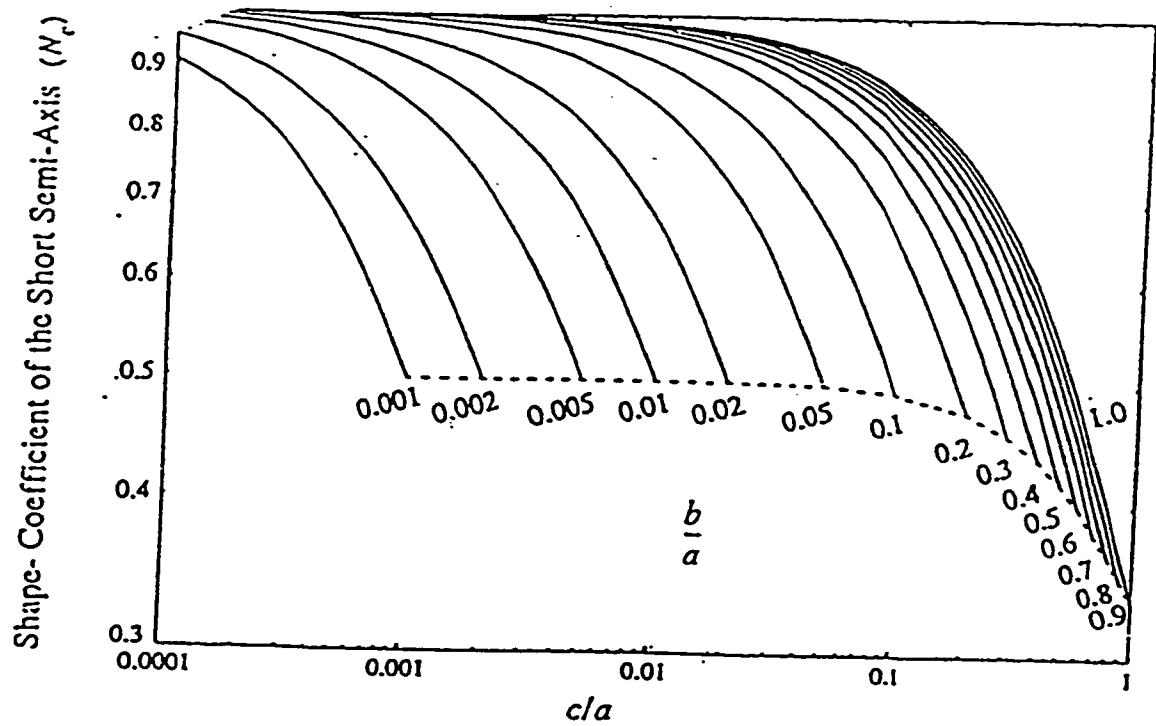


Figure 2.4 Shape coefficient of the general ellipsoid along the short axis N_c

The shape coefficients that we discussed above are for magnetic materials with ellipsoidal shapes. However, the material deposited on our device is rectangular in shape, and the results obtained from an ellipsoid are not completely valid for this shape. Nevertheless, since the thickness of the material deposited on our device is much smaller than the planar size, the difference is mostly in the corner areas; therefore the results obtained from an ellipsoidal shape can still be used to estimate the response of the structure with little error.

If a general rectangular magnetic material has a magnetization M , which makes an angle α with the a semi-axis, an angle β with b semi-axis, and an angle γ with the c semi-axis, then the magnetostatic energy density W is given by [22]

$$W = \frac{M^2}{2\mu_0} [N_a \cos^2 \alpha + N_b \cos^2 \beta + N_c \cos^2 \gamma] \quad (2.10)$$

The magnetic material we deposit on our device has a size of $a = 200 \mu\text{m}$, $b = 260 \mu\text{m}$, and $c = 5 \mu\text{m}$. According to Figure 2.2-2.4, we can find that $N_a = 0.003$, $N_b = 0.002$, and $N_c = 0.995$. Therefore the magnetostatic energies in each direction are

$$W_a = \frac{0.003M^2}{2\mu_0} \quad (2.11)$$

$$W_b = \frac{0.002M^2}{2\mu_0} \quad (2.12)$$

$$W_c = \frac{0.995M^2}{2\mu_0} \quad (2.13)$$

From (2.11) to (2.13), W_c is much larger than W_a and W_b with the same magnetization; this implies that a larger external field is required to magnetize the material in the “c” direction than in the “a” and “b” directions, in which smaller magnetic energies are produced.

To further discuss magnetic anisotropy of the material deposited on our device, we assume that an external magnetic field is applied perpendicular to the “a” axis, which is consistent with the actual operation of our device (Figure 2.5). The material will tend to be magnetized along the direction of the external magnetic field.

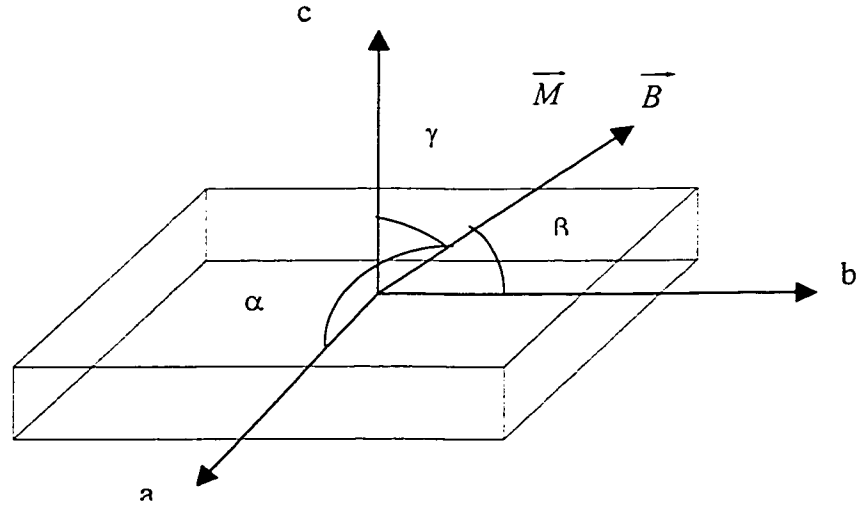


Figure 2.5 Magnetization model of our device

We then have $\alpha = 90^\circ$ and $\sin\beta = \cos\gamma$. The resulting magnetostatic energy density becomes

$$W = \frac{M^2}{2\mu_0} (N_b \cos^2 \beta + N_c \sin^2 \beta) \quad (2.14)$$

Substituting $\cos^2\beta = 1 - \sin^2\beta$, and neglecting constant energy term, we have

$$W = \frac{M^2}{2\mu_o}(N_c - N_b)\sin^2\beta \quad (2.15)$$

where β is the angle that M rotates away from the “b” axis, the longest axis of the material.

Comparing (2.15) to (2.4), the shape anisotropy constant is then given by

$$K_{shape} = \frac{1}{2\mu_o}(N_c - N_b)M^2 \quad (2.16)$$

The material deposited on our device has a saturation magnetization of 0.56 Tesla (See Figure 3.8). The shape anisotropy coefficient of the material deposited on our device is then $1.43 \times 10^5 \text{ J/m}^3$. Compared to the K_{stress} induced by 1.0 GPa stress we quoted before, K_{shape} is three times larger than K_{stress} .

In fact, if a soft magnetic material is designed with a large enough aspect ratio, the shape anisotropy could dominate; the anisotropy contributed by other factors can be neglected. The material is much more easily magnetized along its easy axis (longest axis) than in other directions. This has been demonstrated by measuring the hysteresis curve of our sample Permalloy (refer to Chapter 3).

2. 1. 2 Magnetic Anisotropy Torque

As discussed previously, the total magnetic anisotropy energy density W_{anis} is given by (2.5)

$$W_{anis} = K_{total} \sin^2\phi$$

where K_{total} is the sum of all the anisotropy constants, and ϕ is the angle between the magnetization vector and the easy axis.

Since the magnetic anisotropy energy increases as the magnetization vector rotates away from the easy axis, in order to maintain a minimum internal energy, a restoring torque will be generated, which tends to realign the magnetization with the easy axis. This torque, called the magnetic anisotropy torque, can be obtained by differentiating (2.5)

$$T_{anis} = -\left(\frac{\partial W_{anis}}{\partial \phi}\right)V_{mag} = -2V_{mag}K_{total} \sin \phi \cos \phi = -V_{mag}K_{total} \sin 2\phi \quad (2.17)$$

where V_{mag} is the volume of the magnetic material.

Because of the $\sin 2\phi$ term, the restoring magnetic anisotropy torque increases until it reaches a maximum magnitude at $\phi = 45^\circ$.

2.2 Magnetic Torque

We know that if an ideal permanent magnetic material with a magnetization of \vec{M} is placed at α degree to a magnetic field \vec{B}_{ext} (Figure 2.6), a magnetic torque will be produced on the material. The magnetic torque is formulated as

$$T_{mag} = V_{mag} | \vec{M} \times \vec{B}_{ext} | = V_{mag} M B_{ext} \sin \alpha \quad (2.18)$$

where V_{mag} is the volume of the material.

The magnetic material we deposited on our device is a “soft” magnetic material, far from an ideal permanent magnetic material; (2.18) is not generally applicable for this material. However, if the material is deposited so that the magnetization vector does not or slightly rotates away from its equilibrium position, easy axis. The material will act more like a permanent magnetic material. (2.18) could still be used to estimate the magnetic torque produced by a “soft” magnetic material.

In (2.18), the magnetization (\mathbf{M}) and magnetic field (\mathbf{B}_{ext}) have units of A/m and Tesla, respectively. However, measuring the hysteresis curve of the material deposited on our device gave the magnetization (\mathbf{M}) in units of Tesla. We therefore modify (2.18) as

$$T_{mag} = V_{mag} M B_{ext} \sin \alpha = V_{mag} (M/\mu_0) B_{ext} \sin \alpha = V_{mag} | \vec{M} \times \vec{H}_{ext} | \quad (2.19)$$

where M has units of Tesla, and H_{ext} has units of A/m.

As we discussed in Section 2.1, it is easiest to magnetize a magnetic material along its easy axis. However, the magnetization of the material could be away from its easy axis if an external magnetic field is applied in this direction. If the magnetization direction changes, the microstructure will abruptly relax to a new equilibrium position with a smaller equilibrium torque, therefore a smaller angle of mechanical deflection. It is interesting to discuss how much the magnetization will rotate away from the easy axis corresponding to the external magnetic field being applied.

Figure 2.7 shows a magnetic material magnetized by an external magnetic field \mathbf{B} . \mathbf{B} is at an angle θ to the easy axis of the material, and the magnetization \mathbf{M} is then at an angle ϕ from the easy axis.

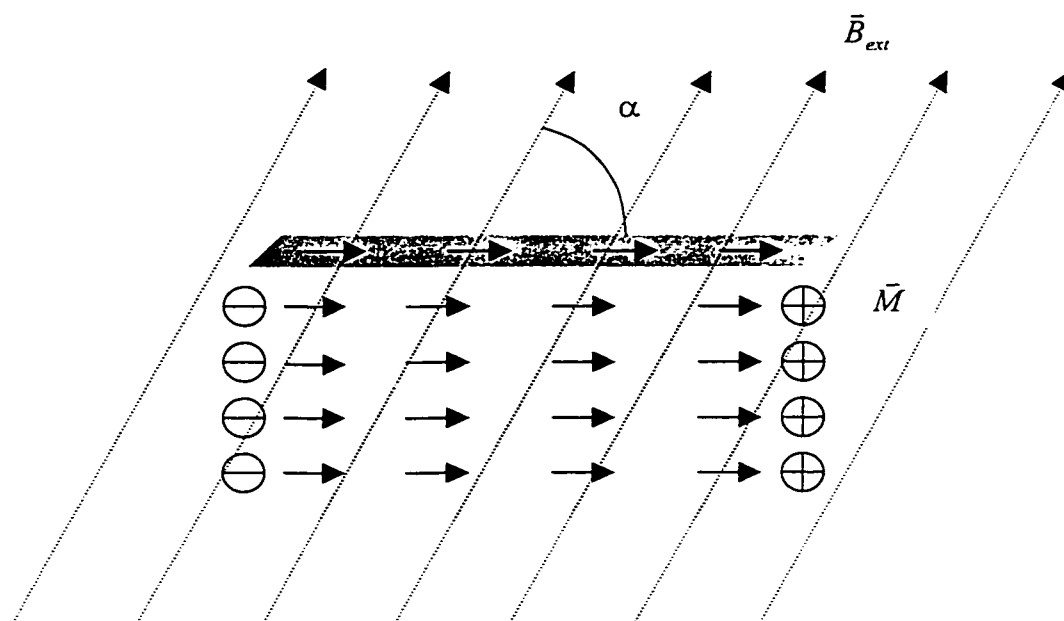


Figure 2.6 A permanent magnetic material with α degree to an external magnetic field \vec{B}_{ext}

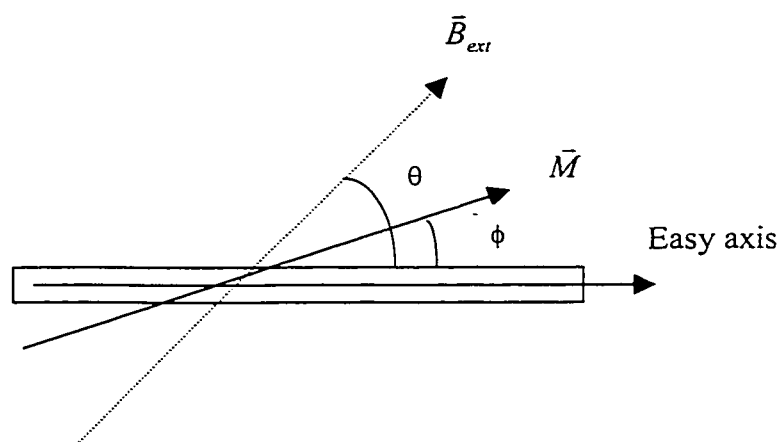


Figure 2.7 Magnetization of a magnetic material under a Magnetic Field

According to (2.19), a magnetic torque will be produced, and expressed as

$$T_{mag} = V_{mag} M H_{ext} \sin (\theta - \phi)$$

Since M rotates away from the easy axis of the material, a magnetic anisotropy torque will be produced, and tend to realign the magnetization with the easy axis. According to (2.17), the magnetic anisotropy torque is

$$T_{anis} = - V_{mag} K_{total} \sin 2\phi$$

At equilibrium, the magnetic anisotropy torque balances the magnetic torque. We then have

$$V_{mag} M H_{ext} \sin (\theta - \phi) = | - V_{mag} K_{total} \sin 2\phi | \quad (2.20)$$

where $H_{ext} = \frac{B_{ext}}{\mu_o}$.

Due to the specially designed shape of the magnetic material deposited on our device, the shape anisotropy energy dominantes among all anisotropy energies, and so we assume $K_{shape} \approx K_{total}$.

A computer program was written in Visual Basic to solve (2.20), and the results are plotted in Figure 2.8. The numbers in the right of Figure 2.8 indicate the angle between the magnetic field and the easy axis (θ).

We can see from Figure 2.8, if the external magnetic field applied to magnetize the material is not too large (less than 100 Gauss), even with a large θ , the magnetization vector will not rotate away from its easy axis very much (less than 1°). The “soft” magnetic material acts somewhat like a “hard” material (only at the point of magnetization direction). In this thesis, the magnetic field used to actuate our device is very small, we assume the magnetization of the magnetic

material deposited on our device will not rotate away from the longest side, which is the easy axis.

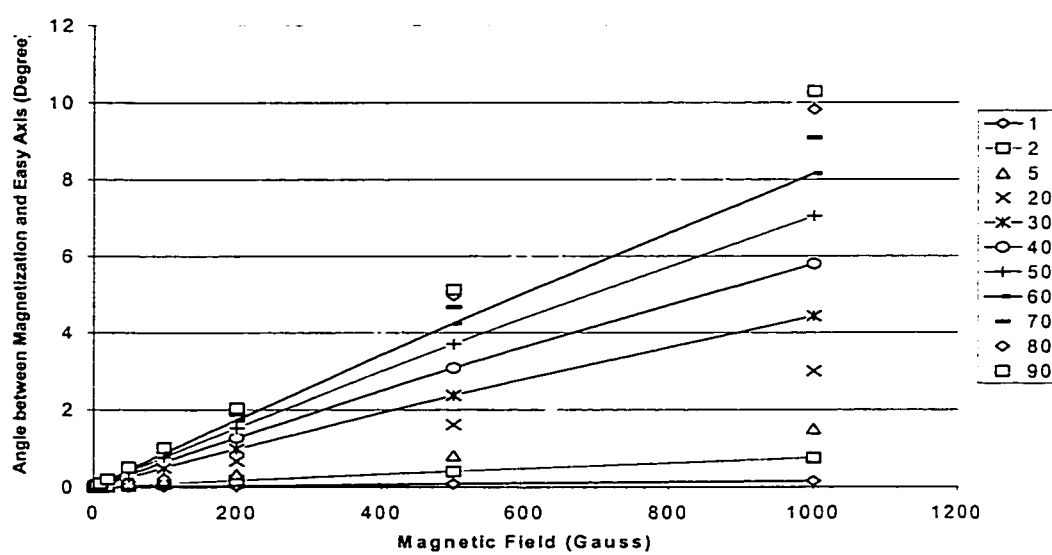


Figure 2.8 Angle between the Magnetization and the Easy Axis
Versus External Magnetic Field

Chapter 3

FABRICATION

This chapter will discuss the electroplating technology and the fabrication process in detail. Firstly, the electroplating process will be discussed, and some important factors involved in this process will be analyzed. Secondly, the fabrication process flow will be outlined; both cross-section and top view figures of the devices will be used to simplify the explanation of the fabrication.

3. 1 The Selection of Magnetic Materials

The magnetic materials most commonly used in micro-fabrication include nickel, iron, cobalt and their alloys with other materials such as chromium and platinum. In this thesis, Permalloy, a nickel-iron alloy (NiFe), is selected due to its well-understood material properties.

The magnetic properties of NiFe are strongly determined by its atomic composition, and then impact on the performance of devices. Figure 3.1 is the curve of the saturation magnetization of NiFe versus percentage of nickel in iron. From this curve, we can see that, the lower the percentage of nickel, the higher the saturation magnetization, except for a minimum at 30% nickel. However, materials with low percentage of nickel tend to be easily corroded, and are not widely used in practical applications.

Two commonly used compositions are 50% nickel in iron ($\text{Ni}_{50}\text{Fe}_{50}$) and 80% nickel in iron ($\text{Ni}_{80}\text{Fe}_{20}$). The former has the highest local saturation magnetization; however, the internal stress of $\text{Ni}_{50}\text{Fe}_{50}$ also reaches a local maximum. $\text{Ni}_{80}\text{Fe}_{20}$ is the most commonly used material in MEMS applications because of its good physical properties and a minimized internal stress.

In this research, both $\text{Ni}_{80}\text{Fe}_{20}$ and $\text{Ni}_{50}\text{Fe}_{50}$ are employed by varying the plating conditions. Figure 3.2 are photographs of $\text{Ni}_{80}\text{Fe}_{20}$ and $\text{Ni}_{50}\text{Fe}_{50}$ samples taken under a microscope. The pictures show that the $\text{Ni}_{80}\text{Fe}_{20}$ sample has a good plating quality with no buckling observed; however, buckling is present at the corner of the $\text{Ni}_{50}\text{Fe}_{50}$ sample, probably because of internal stress.

To minimize the internal stress of the device due to the magnetic material, only $\text{Ni}_{80}\text{Fe}_{20}$ is deposited on the microplatform structure for our subsequent measurement.

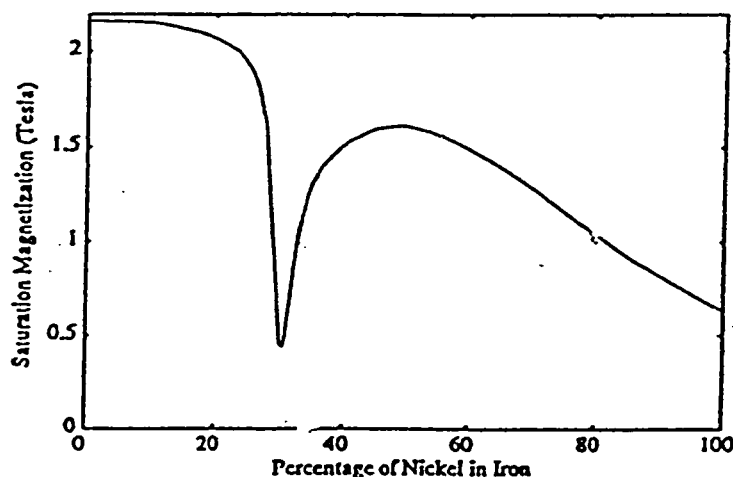
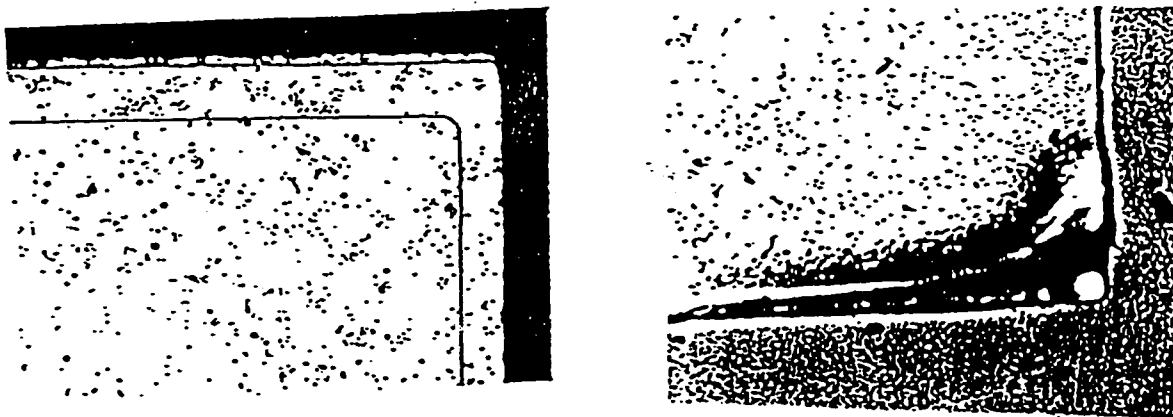


Figure 3.1 Saturation magnetization versus percentage Nickel in Iron [24]

(a) $\text{Ni}_{80}\text{Fe}_{20}$ sample(b) $\text{Ni}_{50}\text{Fe}_{50}$ sampleFigure 3.2 Micrographs of $\text{Ni}_{80}\text{Fe}_{20}$ and $\text{Ni}_{50}\text{Fe}_{50}$ samples

3. 2 The Electroplating of NiFe

Like the traditional electroplating process, electroplating a NiFe alloy also requires an anode, a cathode, a current source, and nickel and iron ions contained in the electroplating bath. The anode used in our research is a meshed platinum electrode; the cathode is a silicon wafer with a composite Cr-Au seed layer coated on it.

Because only specific areas of the wafer are to be electroplated (called selective plating), a thick photoresist layer is applied onto the seed layer and patterned so that electroplating can only take place in the exposed areas (Figure 3. 3).

The current source supplies current from the anode to the cathode through the plating bath. At sufficiently high current density, nickel, iron and hydrogen ions in the plating bath are driven toward the cathode and capture electrons there to produce the NiFe alloy and hydrogen gas. The NiFe alloy will deposit on the surface of the cathode, and hydrogen gas will be given off.

With the reduction of the positive ions, a depletion region will form in the vicinity of the cathode; the positive ions in the main body of the bath will then move to the depletion region by diffusion. The diffusion rate depends on the difference of the ions' concentration between the main body of the bath and the depletion region. If the diffusion rate is less than the reduction rate of the metal ions, the deposition rate will reduce, and the composition of the Ni and Fe will change within the film thickness as well. For practical plating, high concentrations of nickel ions and iron ions are necessary to maintain proper diffusion rates.

Since the electroplating conditions will significantly affect the properties of the magnetic material, here we give a more detailed discussion of each individual factor that affects the characteristics of the NiFe alloy.

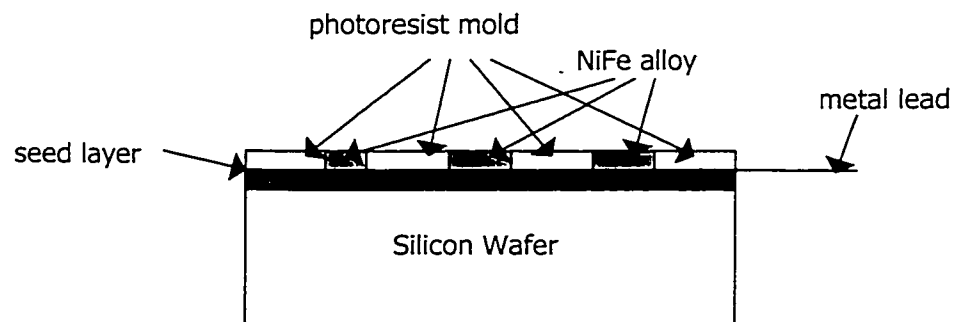


Figure 3. 3 Cross-section of the selective electroplate

Electroplating Bath

A plating bath is a mixed chemical solution that contains the metal ions to be deposited. We define the following components:

Cations: positive metal ions in the bath

Anions: negative ions in the bath

Additive: chemicals added to the plating bath for special purposes

The cations we employed in this work are nickel and iron ions. Each of those has the standard potential of -0.25V and -0.44V respectively. Other positive ions existing in the plating bath are hydrogen ions.

Iron ions are more readily reduced than nickel ions. Thus the ion ratio of Fe to Ni is kept small relative to the atomic ratio desired at the plate. We have the ratio of Fe to Ni is 1:28.

The number of anions that can be used in an electroplating bath is very large. The most important anions are sulfate, chloride, fluoroborate, sulfamate, hypophosphite, and cyanide. The selection of the anions depends on the specific properties desired. Sulfamate was reported to plate with high current efficiency for nickel and iron, thus less hydrogen is evolved at the cathode [25]. Some authors found that using a two anion system has the advantage of less internal stress compared to the all-chloride bath [26]. We choose sulfate and chloride anions.

Additives are normally used for special purposes, such as increasing the conductivity of the plating bath and controlling its pH value.

Low conductivity of the plating bath had caused difficulty at first in our experiment due to insufficient voltage compliance of the current source we used. We solved this problem by adding boron acid (HBO_3) to increase the conductivity of the plating bath.

The pH value of the plating bath may affect the plating mechanism. It is especially important when plating a small area where hydrogen ions are

competing with metal ions for reduction. When hydrogen is produced, hydrogen bubbles can stick to the surface of the cathode to prevent further electroplating in these areas. Wetting agents such as a surfactant can be added to the plating bath to remove the hydrogen bubbles from the cathode surface, but how it affects the plating is still unknown. We removed the hydrogen bubbles by rinsing the wafer in de-ionized water every 10 minutes during the electroplating process. This method produced acceptable plating quality.

Another important function of the additive is reduction of the internal stress. In this work, saccharin was used for this purpose.

The plating bath we employed is based on the results given in [24] and the composition is listed in Table 3.1.

Table 3. 1 NiFe plating bath recipe

NiSO ₄ • 6H ₂ O	200 g/L
FeSO ₄ • 7H ₂ O	8 g/L
NiCl ₂ • 6H ₂ O	5 g/L
H ₃ BO ₄	25 g/L
Saccharin	3 g/L

Conditions: pH = 2.5

Temperature = 21 °C

Current Density = 15 mA/cm²

Plating rate = 2.5 μm/hour

Current Density

As we mentioned before, continuous plating depends on the diffusion of the metal ions from the main body of the bath to the depletion region. In some cases, especially with a high current density, the diffusion of the ions may not keep up with the reduction of the cations. This will cause a non-uniform plating rate and composition through the film. To solve this problem, a 50% duty cycle current pulse with a one second period is used instead of a constant current. In the current-high half-period, plating is dominant; in the current-low half-period, the diffusion of the cations is dominant.

Current density also affects the composition of Ni and Fe in the alloy. The mechanism is quite complicated, and depends on the electroplating bath. Reference [27] reported that, in the low current density range (0-12 mA/cm²), the weight percentage of iron in the alloy slightly decreases with increase of the current density. Our work, however, shows a slight increase of iron in the NiFe alloy. Figure 3.4 shows weight percentage of iron in the alloy versus current density applied. The results are measured by SEM analysis of the sample.

A complete circulation of the plating bath is also very helpful to accelerate the diffusion of the ions. We used a magnetic stir bar to agitate the plating bath to help the diffusion of the cations from the main body to the depletion region.

Seed Layer

Since the material used for the device is an insulating material, SiO₂, a metal layer (called the seed layer) is required to be deposited on it to act as a conductive path from the anode to the cathode, and as a nucleation surface for metal growth. Cr-Au compound layers deposited by sputtering are chosen for this purpose. The thickness of the Cr layer is 20 nm, and it is used as an adhesive layer due to its excellent adhesion to SiO₂. A 700nm thick Au layer is deposited on the top of the Cr layer to provide sufficient conductance of the seed layer. The resulting low resistance of the seed layer prevents a non-uniform potential over the wafer.

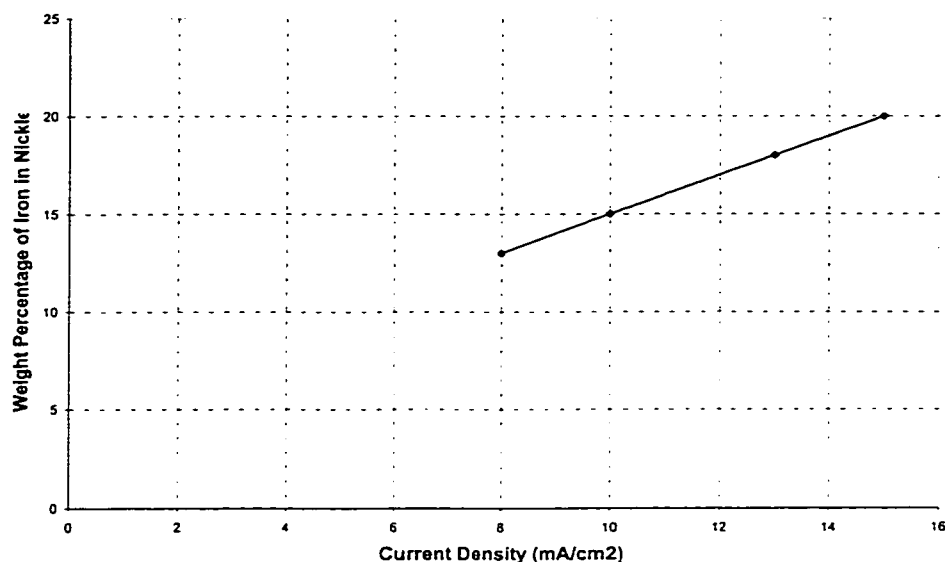


Figure 3.4 Weight percentage of iron in Nickel versus current density

Other Factors

The placement of the anode and the cathode is also very critical for plating high-quality Permalloy. Since the critical mechanism of the electroplating is the electrical field that drives the metal ions to the cathode, a uniform current density onto the whole plated substrate is necessary to make a uniform thickness of the plating material. We placed the anode and the cathode face to face in the plating bath.

However, due to fringe effects and varied size of the plating areas, the current density in the edge areas could be non-uniform. The current lines drawn in Figure 3.5 is actually opposite to the current flowing direction during the electroplating process. We drew this way only for easy understanding.

In order to plate the NiFe alloy as uniformly as possible, the cathode was arranged close to the anode (about 2.0 cm) to improve the uniformity of the electrical field in the central area of the plated wafer.

A step profile probe was used to measure the thickness of the sample Permalloy. Figure 3.6 shows an acceptable thickness uniformity in the central area; however, poor thickness uniformity occurs in the peripheral area at points 4 and 5.

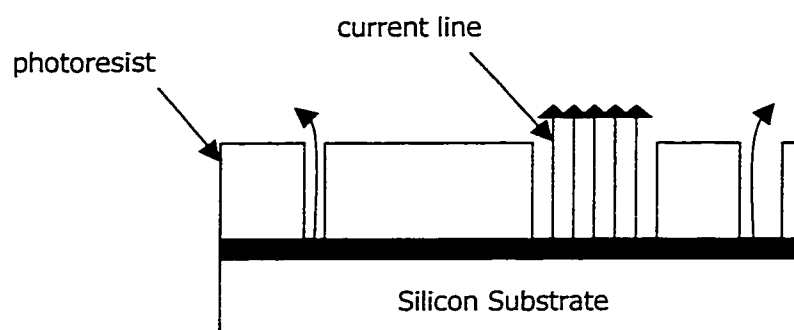


Figure 3.5 Current density through the wafer

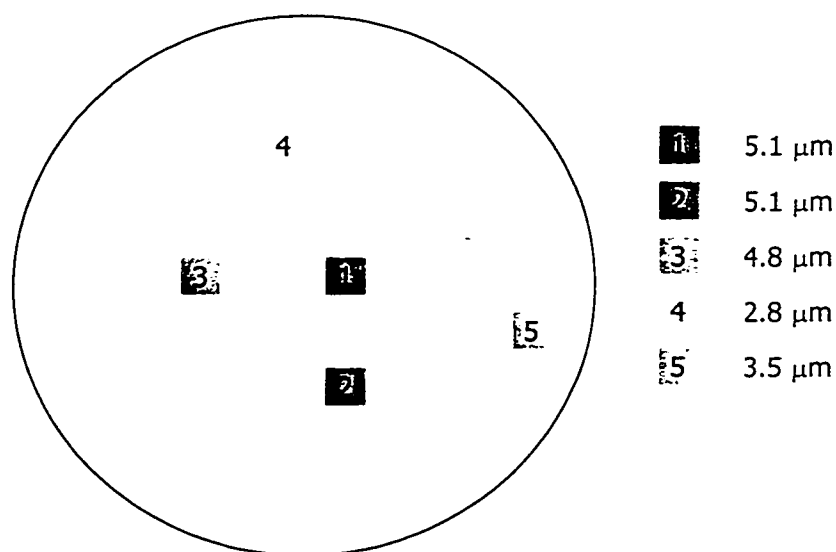
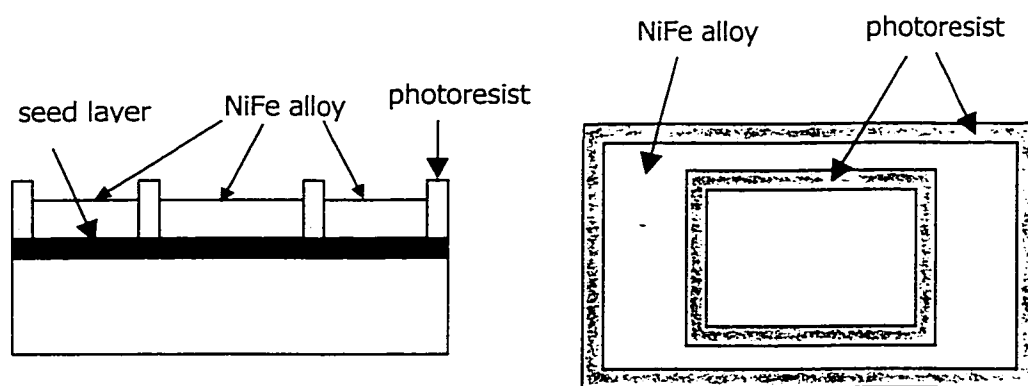


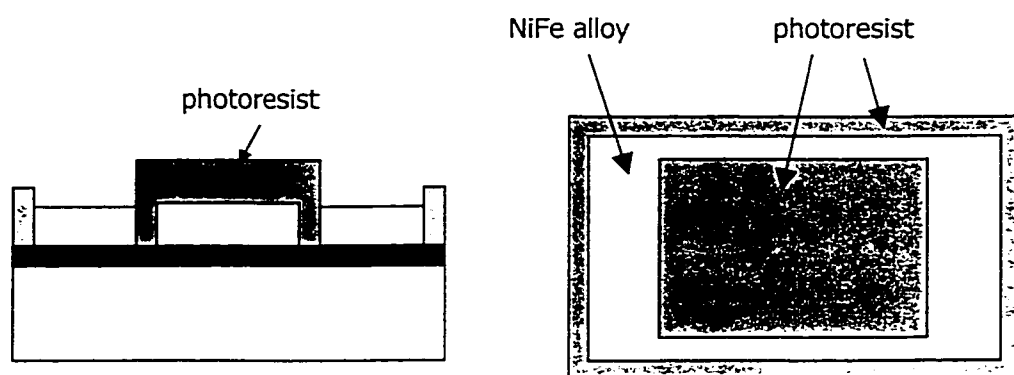
Figure 3.6 Thickness of the NiFe on the wafer

A new technique, called frame plating, and developed by the thin film magnetic recording head industry, allows us to obtain a uniform and well-defined deposition rate. Unlike the selective plating technique, the frame plating technique, shown in Figure 3.7, requires two mask steps. In the first step, the photoresist mold only outlines the desired shape of the magnetic material (Figure 3.7a). Since the insulating plating mold only covers a small portion of the total plating area, the current density is very uniform over the entire plating area and easier to calculate. After having done the electroplating, the second photoresist layer is deposited and patterned so that only desired plating areas are covered with photoresist; the rest of the Permalloy is etched away.

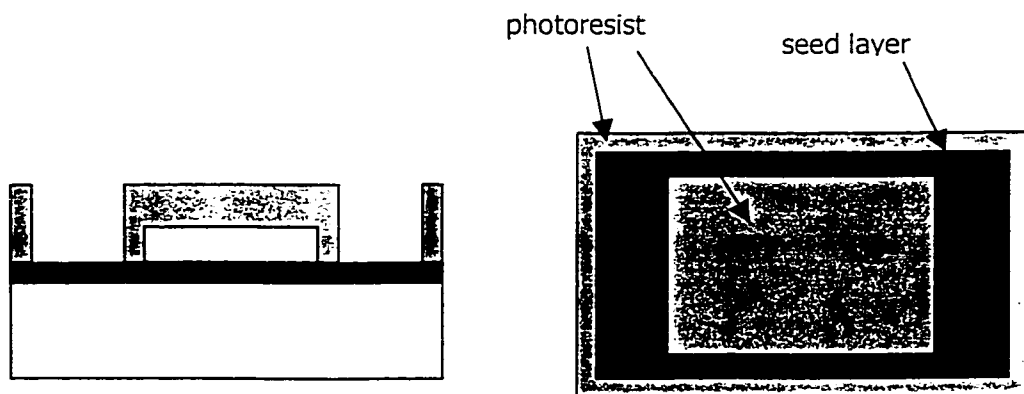
However, in this work, in order to save one mask, the selective plating technique is used, and the central area shows sufficiently good uniformity (Figure 3.6).



(a)



(b)



(c)

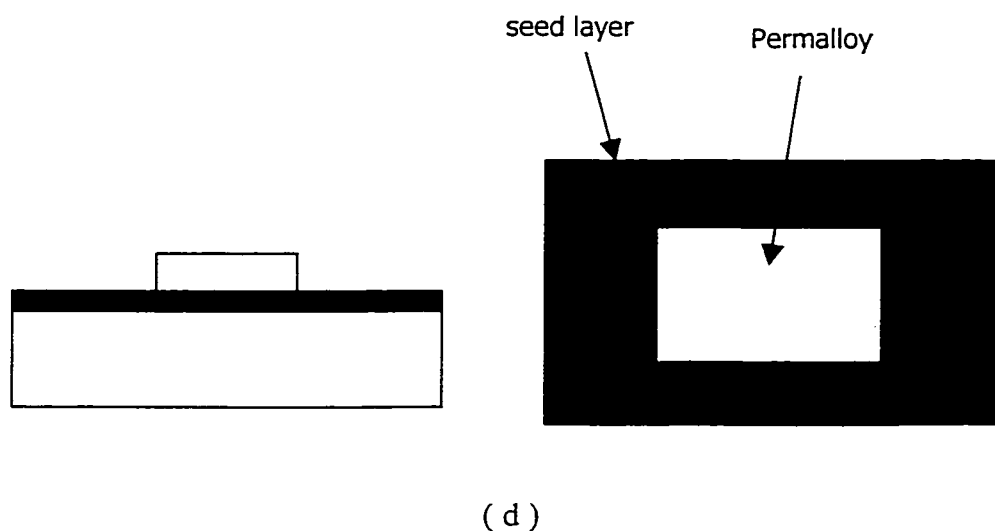


Figure 3.7 The fabrication process of the frame plating technique

3.3 The Characteristics of the Electroplated NiFe Alloy

The most important characteristics of the NiFe alloy include: (1) saturation magnetization, in which all the magnetic dipoles of the Permalloy are lined up, and the magnetization of the Permalloy reaches to maximum; (2) remnant magnetization: the magnetization of the Permalloy when the external magnetic field is removed after completely magnetizing the Permalloy; and (3) the coercive force, the reverse external magnetic field needed to demagnetize the Permalloy to zero.

The NiFe samples deposited on our devices have been tested by a magnetometer manufactured by Quantum Design. Figure 3.8 plots the hysteresis curve of the NiFe sample magnetized along its longest side. The sample has a

saturation magnetization of 0.56 Tesla, coercive force of 3 Gauss and remnant magnetization of 0.22 Tesla. Figure 3.9 is the hysteresis curve of the NiFe alloy along its shortest side (through the depth). From figure 3.9, we can see that the magnetization of the Permalloy magnetized perpendicular to the plate is one order of magnitude smaller than that along the longest side. This result supports the analysis of shape anisotropy we discussed in Chapter 2. The electroplated Permalloy is successfully used as a source to actuate the microstructure in this thesis.

3.4 The Electroplating of a Standard CMOS-processed Device

With the recent development of standard CMOS-processed micro-mechanical devices, electroplating NiFe on standard CMOS-processed devices is an interesting possibility of expanding their potential applications. As part of this thesis, the possibility of electroplating NiFe on standard CMOS processed devices is investigated. The device chosen for this purpose is a CIC device designed by my colleagues [11] and fabricated using the Nortel 1.2 μm CMOS process. The structure of the CIC device is basically a mirror plate supported by triple cantilever arms (Figure 3.10).

As we have seen, electroplating NiFe alloy on microstructures requires some special processes such as a thick photoresist layer to define plating areas. In the standard CMOS process, however, no extra photoresist mold can readily be used as the devices shipped to us are already cut into a small dice. Therefore some special design is required to electroplate Permalloy on the standard CMOS-processed devices.

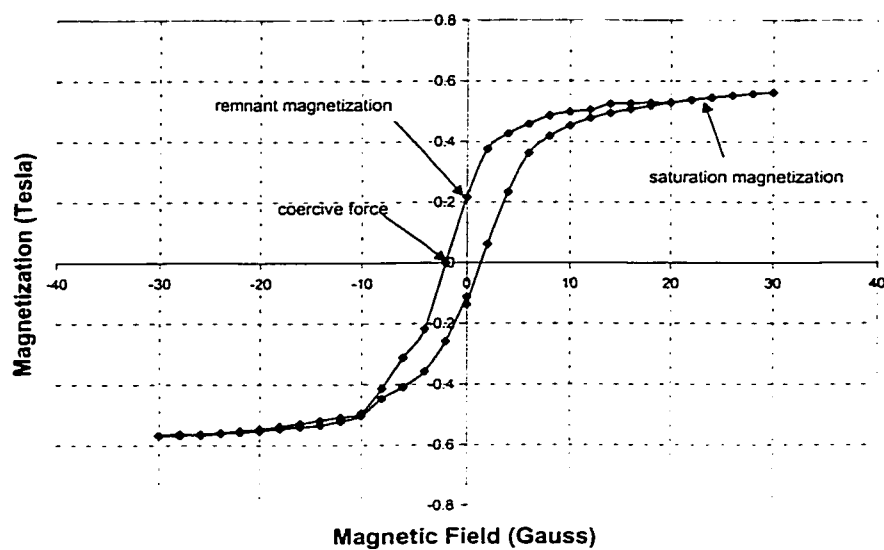


Figure 3.8 Hysteresis curve of the plated NiFe alloy along longest side

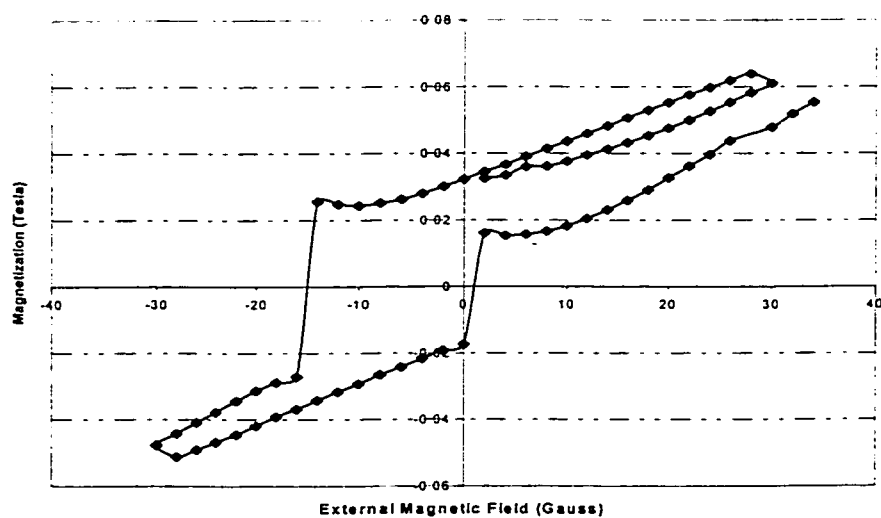


Figure 3. 9 The hysteresis curve of the plated NiFe alloy along the shortest side

The passivation layer provided by the Nortel 1.2 μm CMOS process has a thickness of $\sim 2 \mu\text{m}$. It can be used as an electroplating mold to define the electroplating areas. The aluminum layer underneath the passivation layer can be used as a seed layer. Therefore the device is designed by omitting the passivation layer on the central mirror area during the CMOS manufacture, thus exposing the aluminum layer. Aluminum leads are routed through the arms from the central mirror to a pad, and the device is then glued on a glass substrate. Finally, a wire is bonded to the pad to make an electrical connection from the pad to the cathode. Because the thickness of the passivation layer is only about 2 μm , the thickness of the Permalloy to be electroplated is limited. The electroplating conditions are the same as those introduced before.

We observed the electroplating sample using a microscope, and saw well-defined plating geometry on the central mirror. But Permalloy was also seen at some supporting arm areas. Because the aluminum leads in the arm areas are too close to the edge of the arms; apparently the electrical leakage through the edges of the arms permitted electroplating in these regions.

Due to limited time, only a preliminary investigation has been done, and extensive work is needed to carry on. But these experimental results have shown the possibility to use this technology to expand the potential applications of standard CMOS processed-micromechanical devices.

3.5 The Fabrication of the Devices

Fabrication of the devices starts with a 4 inch p-type (100) silicon wafer. Firstly, a 1.0 μm thick SiO_2 layer is thermally grown on the wafer. The SiO_2 layer acts as the structural material of the device, and as a mask for the subsequent release of the structures from the silicon substrate. Although a few structures were designed, here we only use a single cantilever structure as an example to explain each fabrication step.

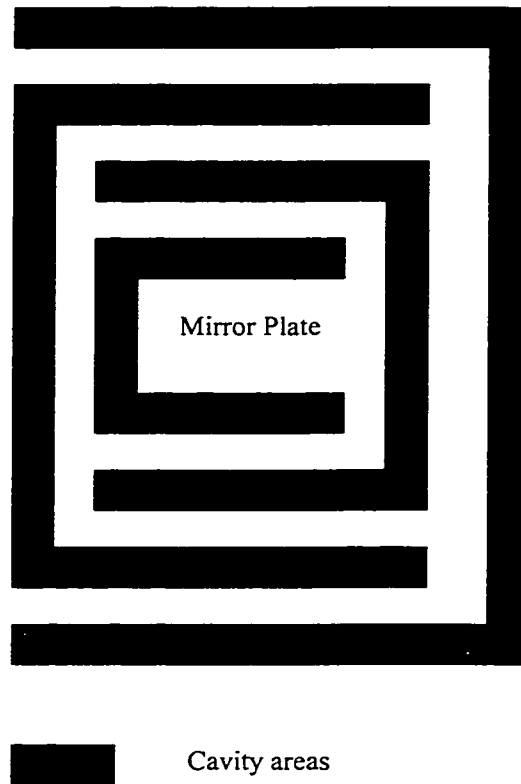


Figure 3.10 Top view of the CIC device

Secondly, the SiO_2 layer is patterned to define the outline of the device (Figure 3.11a); the SiO_2 that is not covered by photoresist is etched away, leaving open areas for an anisotropic etch at the end of the fabrication process (Figure 3.11b).

A 20-nm-thick chrome layer and a 700-nm-thick gold layer are then deposited consecutively on the wafer by sputtering. The thin chrome layer improves the adhesion of the gold to the SiO_2 , while the thick gold layer provides good conductance for the electroplating of the magnetic material NiFe alloy.

A photoresist layer then covers the wafer and is patterned to define the areas intended to be plated (Figure 3.11c). Since a NiFe layer of thickness $5\text{ }\mu\text{m}$ or more is required to produce a large enough torque when the device interacts with the external magnetic field, the photoresist layer in this step must be even thicker so that the plated NiFe is well defined. A viscous photoresist is used in this work, with a thickness of around $15\text{ }\mu\text{m}$. The wafer is then ready for the next step, which is electroplating the NiFe alloy. The details of the electroplating process have been introduced in Section 3.1.2.

After electroplating a $5\text{-}\mu\text{m}$ -thick NiFe layer, the photoresist is removed by dissolving it in acetone (Figure 3.11d). Because the chrome etchant also etches NiFe, the thick photoresist is again deposited and patterned to cover the NiFe alloy to protect it (Figure 3.11e). The uncovered chrome and gold layers are etched away by wet etching, and the photoresist on the NiFe alloy is then removed.

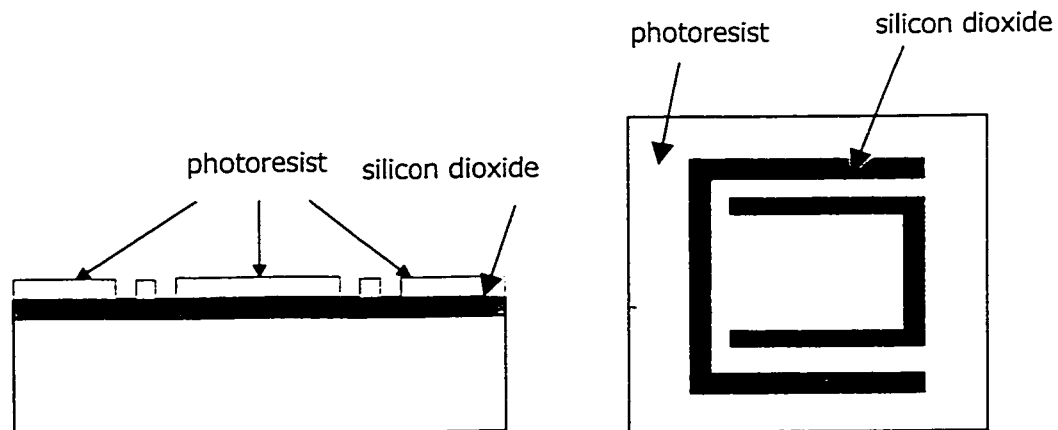
The last step is to release the structure from the silicon substrate by an anisotropic etch (Figure 3.11f).

The mechanism of the anisotropic etch relies on the fact that a silicon crystal is an anisotropic material. The atomic densities in the various crystal orientations are different, resulting in different etch rates along the different crystal orientations. The three major crystal orientations of silicon are $\langle 100 \rangle$, $\langle 110 \rangle$ and $\langle 111 \rangle$, and the etch rates in the $\langle 100 \rangle$ and $\langle 110 \rangle$ directions are much faster than that in the $\langle 111 \rangle$ direction. To etch a concave pattern (interior of a masked pattern) of a (100) silicon, the crystal plane eventually exposed is that

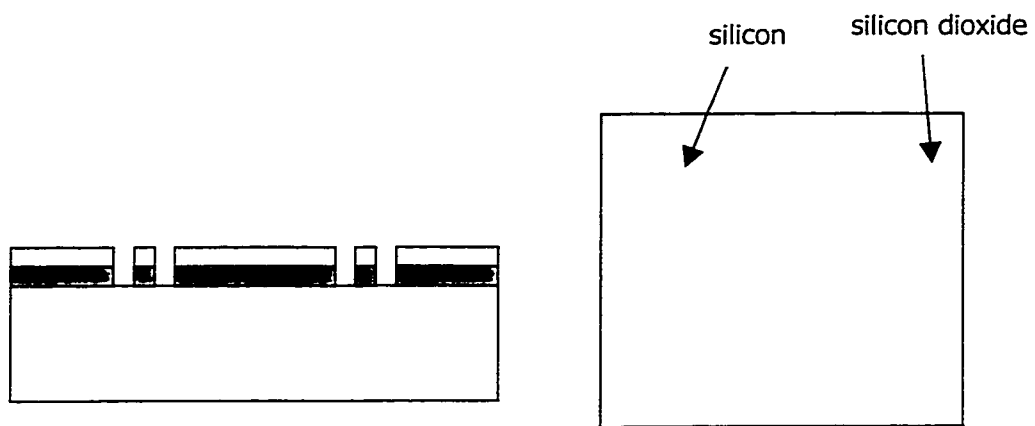
which has the slowest etch rate, (111); to etch a convex pattern (exterior of a masked pattern), however, the exposed crystal plane is that which has the fastest etch rate, (221).

In this device, the edge of the micromirror is aligned along $\langle 110 \rangle$ direction. The corners of the mirror are convex patterns. When etching the device, the (221) plane will be exposed at the corners, causing undercuts (Figure 3.12). With a long enough etching time, the silicon under the support arms and the micromirror will be etched away, and the structures are released from the silicon substrate.

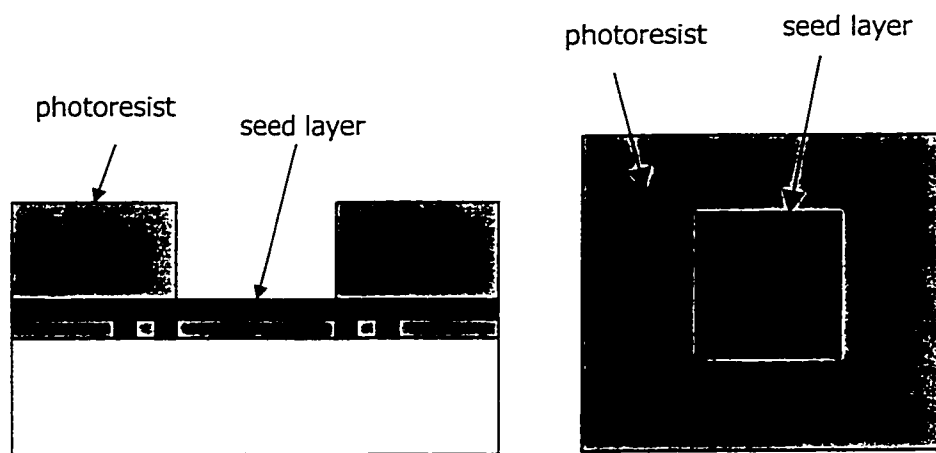
The etchant used to release the mirror is a 5% TMAH with 6 g/L potassium persulfate. Potassium persulfate can dissolve the etching residue remaining on the etch surface, which prevents the further etching of the silicon. The etching temperature is 80°C .



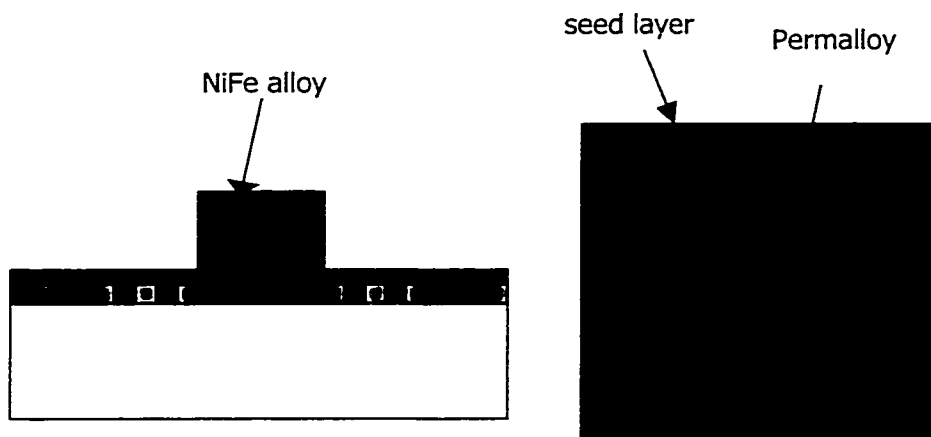
(a)



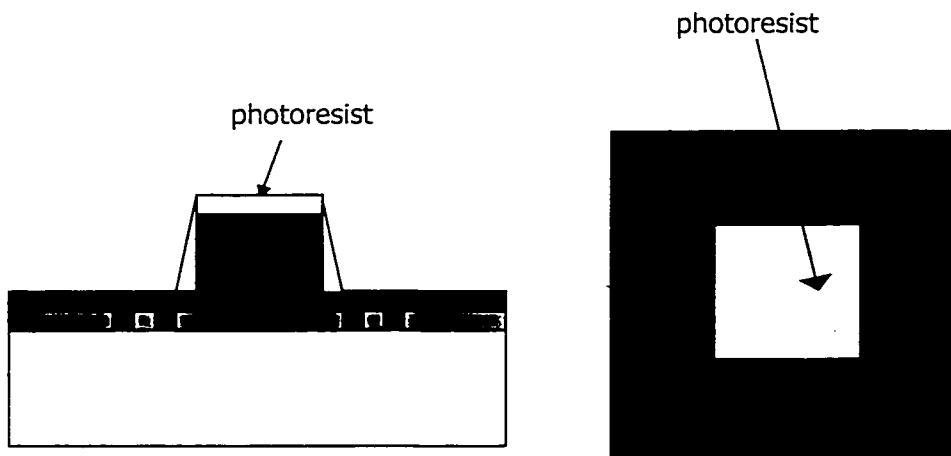
(b)



(c)



(d)



(e)

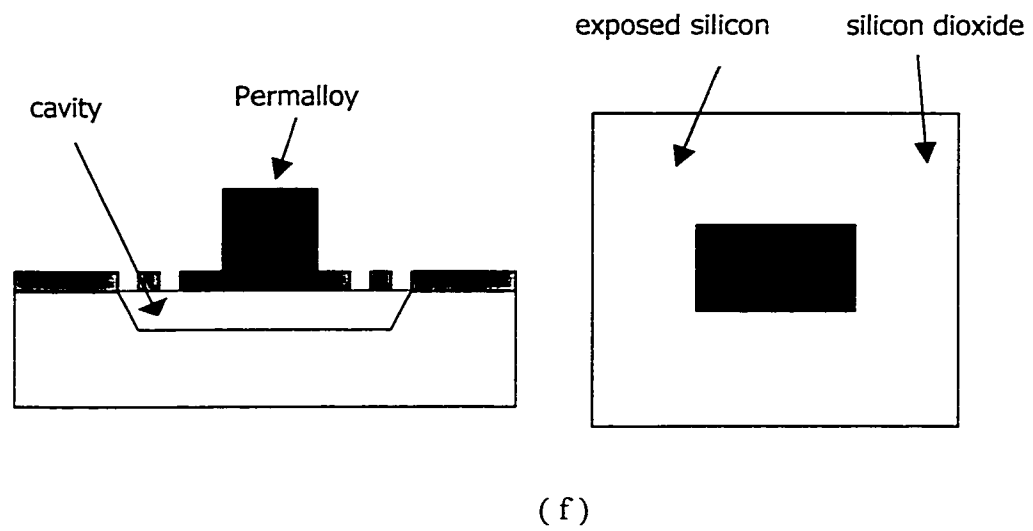


Figure 3.11 Cross-section and top view of the fabrication
Process flow

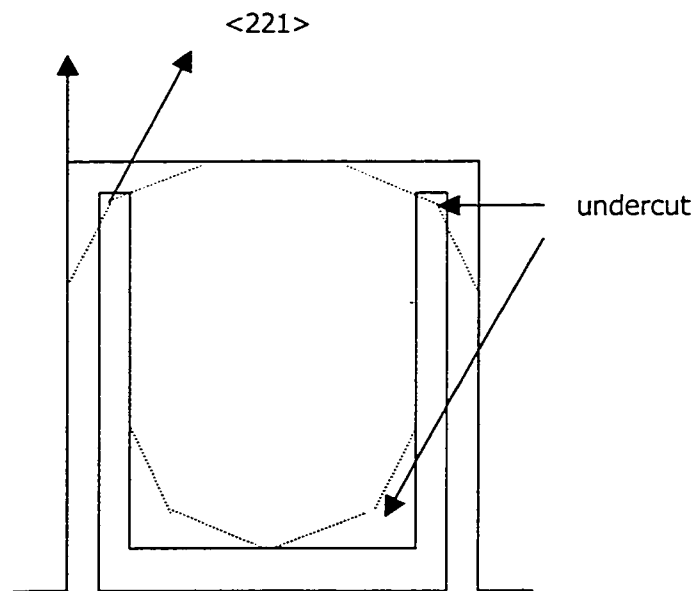


Figure 3.12 Undercut of silicon anisotropic etch

Chapter 4

MECHANICAL ANALYSIS OF THE DEVICE

4.1 The structure of the Device

A few structures have been designed and fabricated in this work. However, in order to simplify the mechanical analysis of the devices, only one structure, which is a rectangular platform supported by two cantilever arms at the far end, is discussed. The material used to construct the platform is thermally grown silicon dioxide with a thickness of 1 μm . On the top of the platform is a 5 μm thick NiFe alloy layer deposited by electroplating. The top view of the device is shown in Figure 4.1. The sizes of the structure indicated in Figure 4.1 are given in Table 4.1:

Table 4.1 Structure Dimension in μm

L	310
W	20
L_{bar}	20
L'	260
W'	200

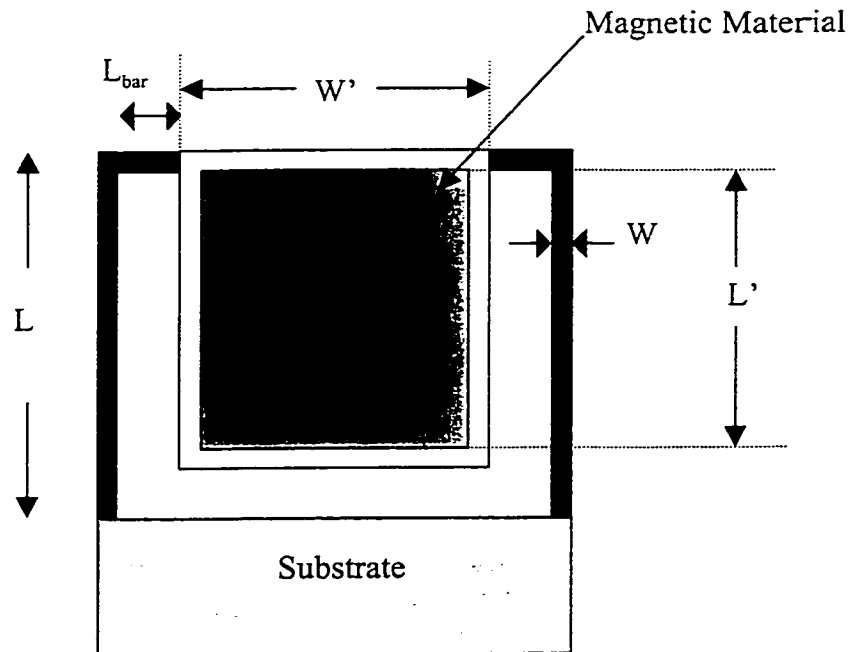


Figure 4.1 Top view of the structure

2. 2 Mechanical Analysis

2. 2. 1 Static Deflection

Before the device is placed in an external magnetic field, the magnetic material is pre-magnetized along its longest axis. The remnant magnetization will interact with the magnetic field applied perpendicular to the platform structure, resulting in a magnetic torque.

The torque generated is given by (2.19):

$$T_{mag} = V_{mag} | \vec{M} \times \vec{H}_{ext} | \quad (4.1)$$

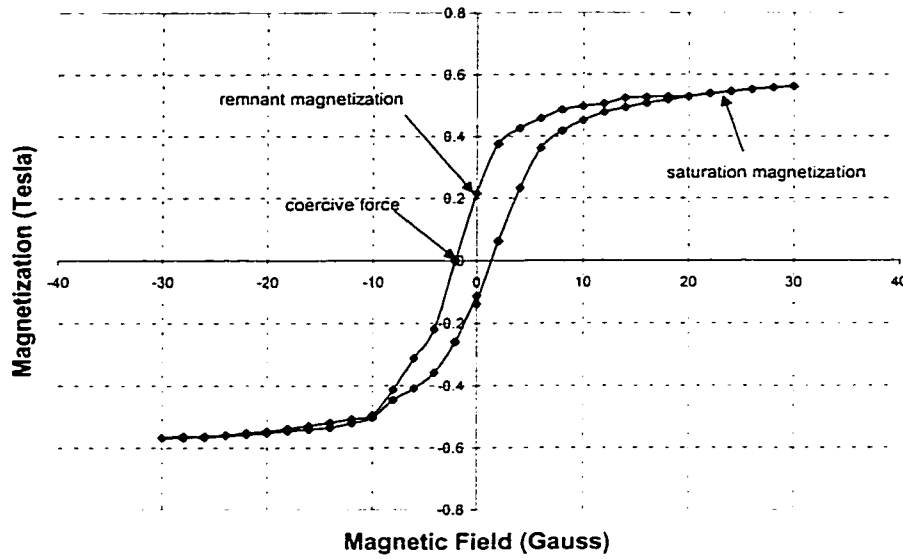


Figure 4.2 Hysteresis curve of the magnetic material along the longest axis

Since the NiFe layer deposited on the platform is much thicker than the support arms, the platform can be considered mechanically rigid. The application of the torque to the ends of the NiFe does not result in the bending of the platform but the bending of the support arms, hence the tilting of the platform (Figure 4.3).

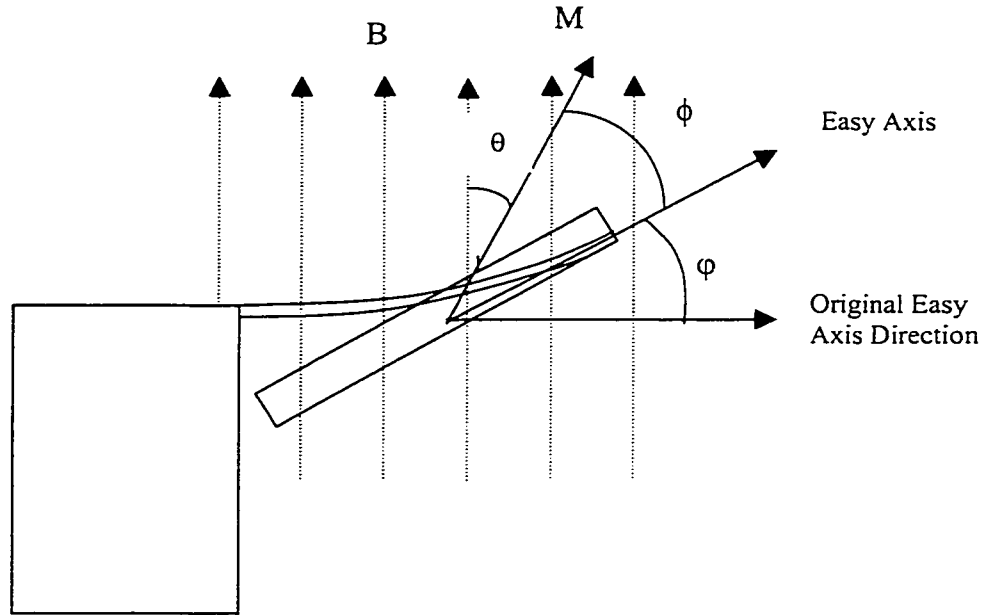


Figure 4.3 Side view of the deflected structure

As the platform tilts, the external magnetic field will tend to magnetize the magnetic material with the same orientation as the magnetic field. However, when the magnetization vector rotates away from its easy axis, a magnetic anisotropy torque T_{anis} is generated, and it attempts to realign the magnetization vector to the easy axis. T_{anis} is given in (2.17) by the formula

$$T_{anis} = -V_{mag} K_{total} \sin 2\phi \quad (4.2)$$

where K_{total} is called the magnetic anisotropy constant; ϕ is the angle formed when the magnetization vector rotates away from its easy axis.

Since the anisotropy torque T_{anis} attempts to bring the magnetization vector back to its easy axis, an equal but opposite torque $-T_{\text{anis}}$ is produced and exerted on the easy axis, and hence on the magnetic material itself. Because the magnetic material is attached to the flexure arms, $-T_{\text{anis}}$ will cause the bending of the support arms. The platform therefore rotates an angle φ from its original easy axis (Figure 4.3).

As the platform rotates, the long arms will bend and the short bars that connect the arms and platform will twist so that a mechanical restoring torque is produced to balance the magnetic torque generated by the magnetic interaction between the NiFe alloy and the external magnetic field. Since the bars connected to the platform are very short compared to the long arms in this design, the mechanical restoring torque contributed by twisting can be ignored. The torque produced by bending the long arms is formulated as [28]

$$T_{\text{mech}} = K_{\varphi} \times \varphi \quad (4.3)$$

where K_{φ} is a constant determined by the geometry and the material properties of the structure.

In equilibrium, the anisotropy torque T_{anis} balances the field torque T_{mag} . In turn, the torque on the magnetic material $-T_{\text{anis}}$ balances the mechanical restoring torque T_{mech} . The resulting equilibrium condition is

$$T_{\text{mag}} = T_{\text{anis}} = T_{\text{mech}} \quad (4.4)$$

Since the external magnetic field is a DC field, the magnetization of the Permalloy is in the region from the remnant magnetization to the saturation magnetization. The relationship between the magnetization of the Permalloy and the external magnetic field is given by curve fitting Figure 4.2 and expressed as

$$M = \left\{ \begin{array}{ll} 0.2272 + 0.089B - 0.012B^2 & 0 < B \leq 8(G) \\ 0.4474 + 0.0028B & 8 < B \leq 30(G) \\ M_s & 31 < B \leq 150(G) \end{array} \right\} \quad (4.5)$$

Substituting (4.1) and (4.3) into (4.4), we have

$$V_{mag} M \times H_{ext} \sin \theta = K_{\varphi} \times \varphi \quad (4.6)$$

where $\theta = 90 - \varphi - \phi$.

As discussed in the Section 2.2, the angle ϕ that the magnetization can rotate away from its easy axis is very small, and is set to zero here.

Therefore

$$V_{mag} M \times H_{ext} \cos \varphi = K_{\varphi} \times \varphi \quad (4.7)$$

According to [28]

$$K_{\varphi} = \frac{EI}{L} \quad (4.8)$$

where E is Young's Modulus of the support arms, L is the length of the arms, and I is the moment of inertia of the cross sectional area of the arms, defined in [29] as:

$$I = \frac{wt^3}{12} \quad (4.9)$$

where w and t are the width and thickness of the support arms, respectively.

Substituting (4.5), (4.8), and (4.9) into (4.7), and because the platform is supported by two arms, the right side of (2.26) needs to multiply 2, we obtain

$$V_{mag} \frac{B_{ext}}{\mu_0} \cos \varphi \left\{ \begin{array}{ll} 0.2272 + 0.0889B - 0.12B^2 & 0 < B \leq 8(G) \\ 0.4474 + 0.0028B & 8 < B \leq 30(G) \\ M_s & 31 < B \end{array} \right\} = 2 \times \varphi \times \frac{Ewt^3}{12L} \quad (4.10)$$

where $V_{mag} = 260 \times 200 \times 5 = 2.6 \times 10^{-13} \mu m^3$, $\mu_0 = 4\pi \times 10^{-7}$, $E = 74 \text{ Gpa}$, $w = 20 \mu m$, $t = 1 \mu m$, $L = 310 \mu m$, and $M_s = 0.56 \text{ Tesla}$

By solving (4.10), the relation between the external magnetic field and the deflection angle of the cantilever can be obtained. The solution is plotted in Figure 4.4.

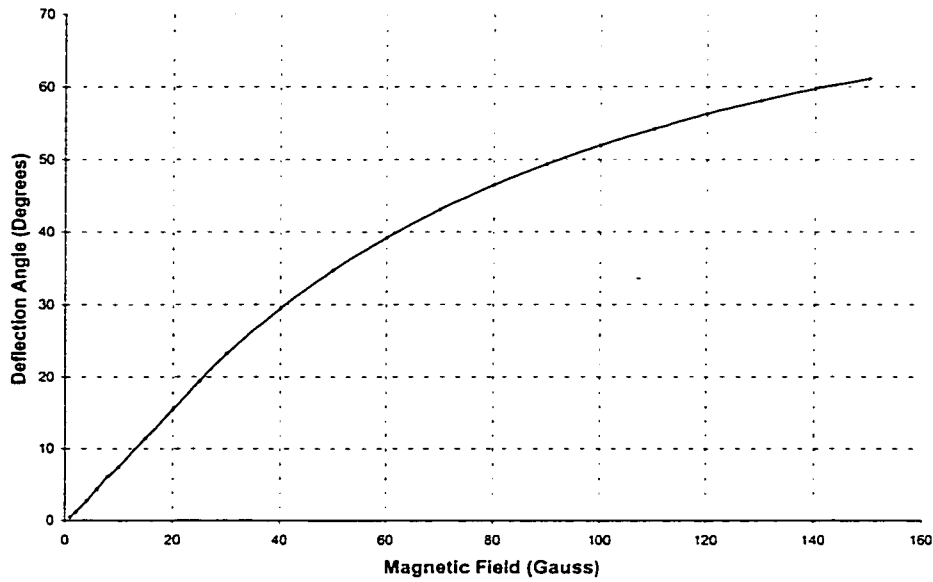


Figure 4.4 Deflection angle versus magnetic field curve
by theoretical calculation

4.2.2 Resonant Response

The deflection of the structure at resonance is not only determined by the torque but also the damping conditions. Assuming that the deflection of the device is governed by the classic equation of linear elasticity, according to [30], we have

$$\rho \frac{\partial^2 z}{\partial t^2} + \rho_l \frac{\partial z}{\partial t} + L(z)z = T(x, y, t) \quad (4.11)$$

and

$$\begin{aligned} L(z) = & \frac{\partial^2}{\partial x^2} [D_x \frac{\partial^2 z}{\partial x^2}] + \frac{\partial^2}{\partial y^2} [D_y \frac{\partial^2 z}{\partial y^2}] + \frac{\partial^2}{\partial y^2} [D_l \frac{\partial^2 z}{\partial x^2}] \\ & + \frac{\partial^2}{\partial x^2} [D_l \frac{\partial^2 z}{\partial y^2}] + \frac{2\partial^2}{\partial x \partial y} [D_{xy} \frac{\partial^2 z}{\partial x \partial y}] \end{aligned} \quad (4.12)$$

where $D_x(x, y)$, $D_y(x, y)$, $D_l(x, y)$, and $D_{xy}(x, y)$ denote the flexural rigidities of the device; ρ is the area density (mass/area); ρ_l is the damping term and T is the torque.

We know from (4.5), that magnetization \vec{M} is the function of the external magnetic field, and the torque is then

$$\vec{T}(x, y, t) = V_{mag} \vec{M} \times \vec{H} \quad (4.13)$$

Although solving (4.11) to (4.12) is possible, it is very difficult. In this thesis, we only use a finite element analysis (ANSYS) to analyze the resonant modes of our devices. Through ANSYS, we found three resonant modes at frequencies of 440.1 Hz, 559.2 Hz, and 1301 Hz.

In the first mode (shown in Figure 4.5) and the second mode (shown in Figure 4.6), the two support arms bend up or down simultaneously, resulting in an up-and-down movement of the platform. The bending regions of the arms are, however, different in these two modes. The arms bend mostly at the end close to the substrate with the first mode, but at the far end with the second mode.

In the third mode (shown in Figure 4.7), two arms bend in different directions. One bends up, the other bends down, resulting in a twisting movement of the platform.

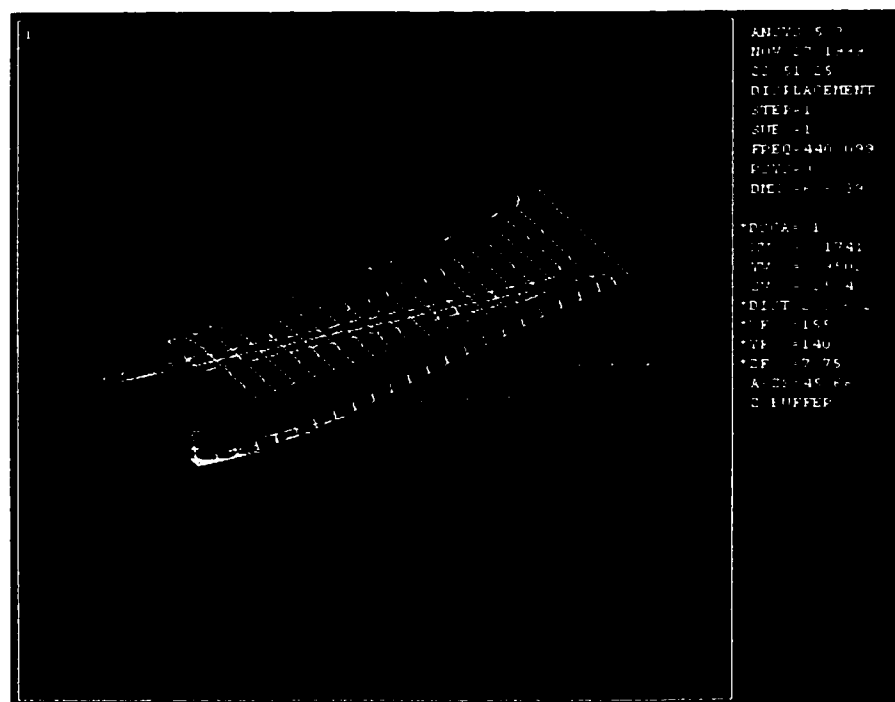


Figure 4.5 The first resonant mode of the device

Chapter 5

EXPERIMENTAL RESULTS AND DISCUSSION

This chapter starts by describing the equipment used to test our device. Next, both static and dynamic angular mechanical deflection measurements are discussed. Finally the experimental results are compared with the theoretical predictions.

5.1 Experimental Equipment

The major equipment used to test the device includes a magnetic field source, a measuring microscope, and a helium-neon laser.

5.1.1 Magnetic Field Source

Since both static and dynamic responses are to be tested, we chose an electromagnet, EMR 175, to produce a magnetic field. The electromagnet is designed to produce a DC magnetic field, and its feature size and the configuration are shown in Figure 5.1. The central shadowed area is the core of the electromagnet, and is the area in which magnetic field is produced. The magnetic field produced by the electromagnet is a function of the current applied to it. However, we measured the voltage applied to the electromagnet, rather than

measure the current. Value of current can be calculated knowing the internal resistance of the coil is $23\ \Omega$.

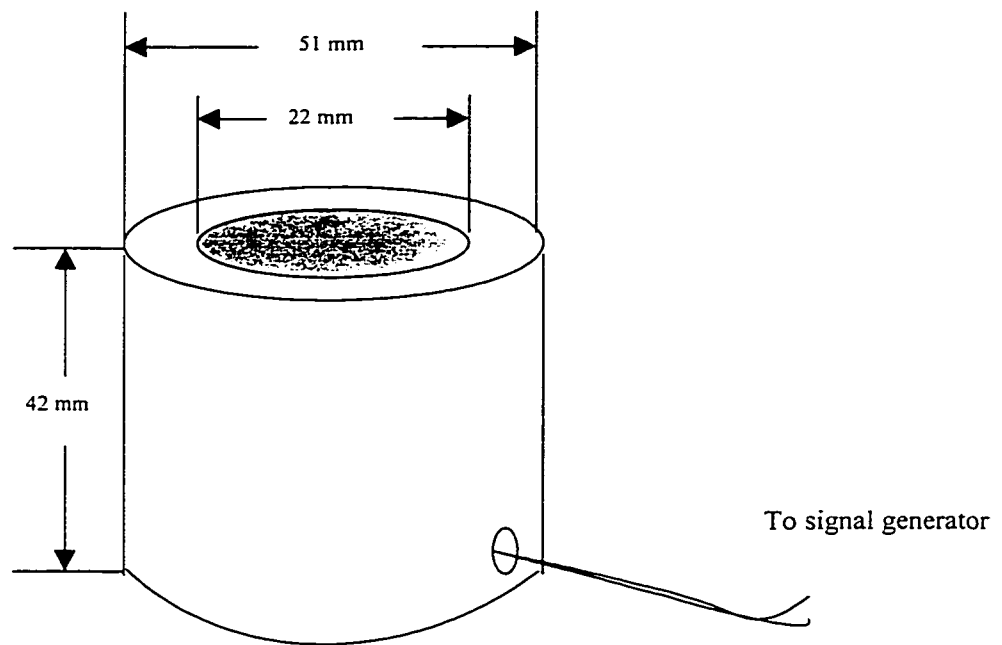


Figure 5.1 Configuration of the electromagnet

A voltage is applied to the electromagnet, the generated magnetic field corresponding to the applied voltage is measured by a gaussmeter, and is plotted in Figure 5.2.

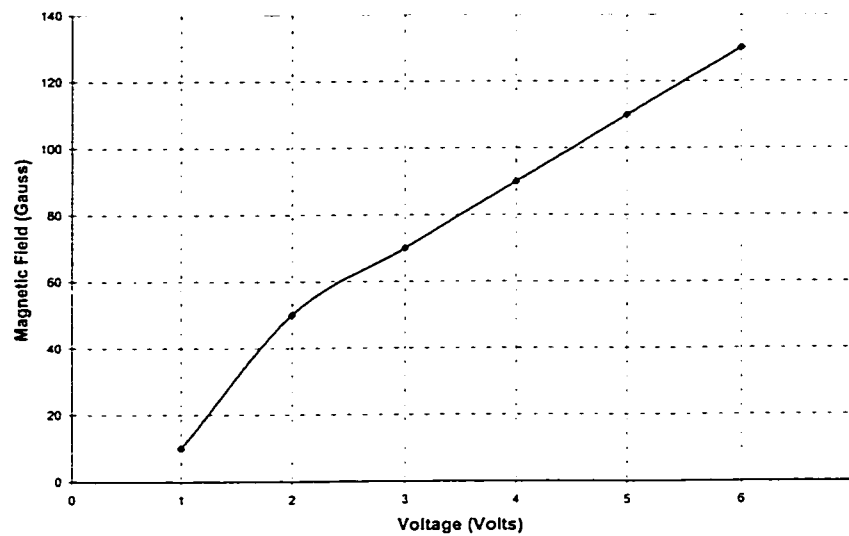


Figure 5.2 Generated magnetic field versus applied voltage

However, if a sinusoidal voltage with fixed amplitude is applied, the peak-to-peak magnetic field will drop dramatically with increasing frequency. The curve of the magnetic field versus frequency with fixed 2 V peak-to-peak magnitude is measured by a gauss meter, manufactured by Lakeshore Inc., and plotted in Figure 5.3. In the dynamic response measurement, since the measurement starts from the frequency of 220 Hz, we have taken account of this effect by rescaling the magnetic field in the ratio of $B(220\text{Hz}) / B(\omega)$.

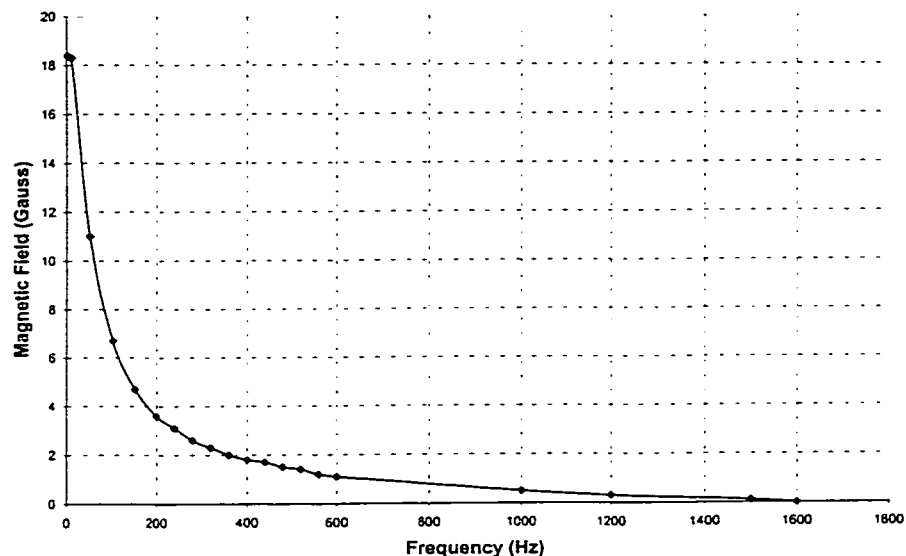


Figure 5.3 Magnetic field versus frequency with 2 V peak-to-peak magnitude

5. 1. 2 Microscope

The microscope used is an Olympus BH2-UMA. It can measure the horizontal distance on the image of the object being examined. Attaching a video camera to the microscope permits the image of the object to be displayed on a TV monitor.

5. 2 Experimental Set-up and Results

Two methods have been used to measure the deflection of the cantilever structure. The first involved measuring the foreshortening of the image of the mirror, and was employed for static deflections. The second involved measuring

the distance traveled by a reflected light spot from a Helium-Neon laser on a screen, and was used for dynamic response measurements.

5.2.1 Static Deflection

In our initial experiment, the pole of a disc-shaped permanent magnet with the maximum magnetic field of 0.2 Tesla was positioned under the device and moved around. This resulted in a magnetic field whose direction and magnitude could be changed. Observation showed the deflection well beyond 90° to the substrate plane. Hence large static deflections are readily attainable.

For quantitative measurement, the device was glued on the electromagnet center and placed under the microscope. When a magnetic field was applied, the mirror deflected. The deflection was calculated according to a simplified model shown in Figure 4.4, and is described below:

The relative length of the image of the mirror is directly measured from the TV screen; without deflection, the length is L ; with a certain amount of deflection, the length changes to L' . The deflection angle θ is then calculated using (5.1)

$$\theta = \cos^{-1}\left(\frac{L'}{L}\right) \quad (5.1)$$

To compare the experimental results with the theoretical prediction previously given in Chapter 4, we combine two results in a single graph in Figure 5.5. With the indication of 10% vertical bar, we can see that the theoretical predictions match the experimental results (within 10%) except for the first point.

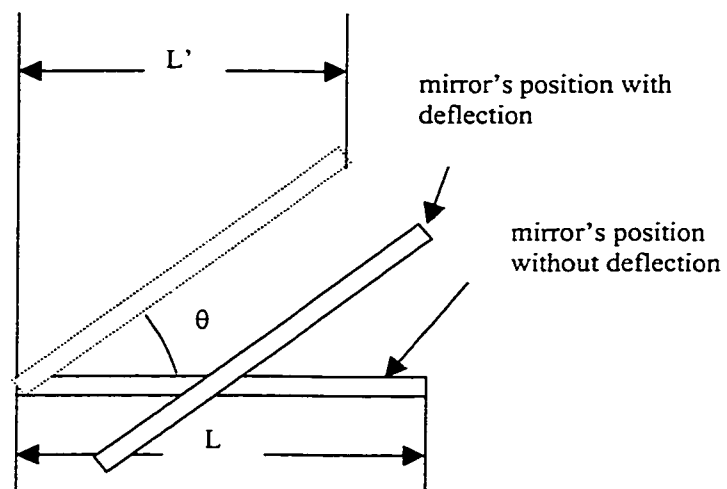


Figure 5.4 Simplified model for static deflection calculation

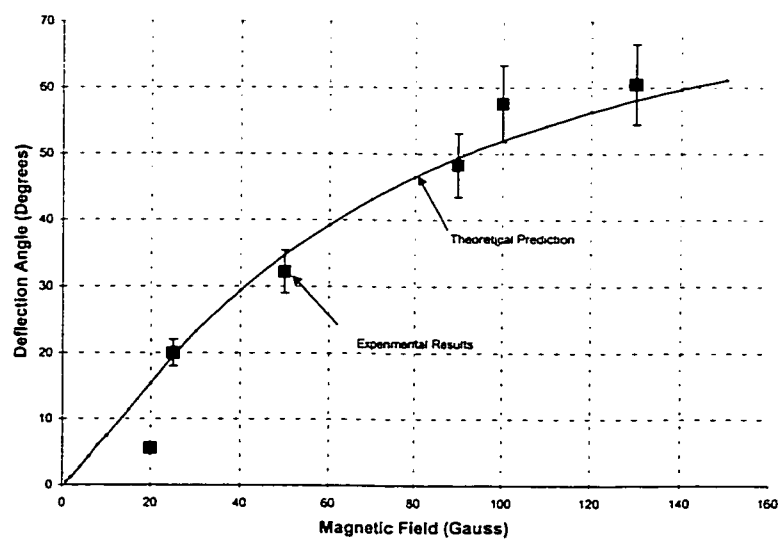


Figure 5.5 Comparison of the experimental and theoretical static deflection

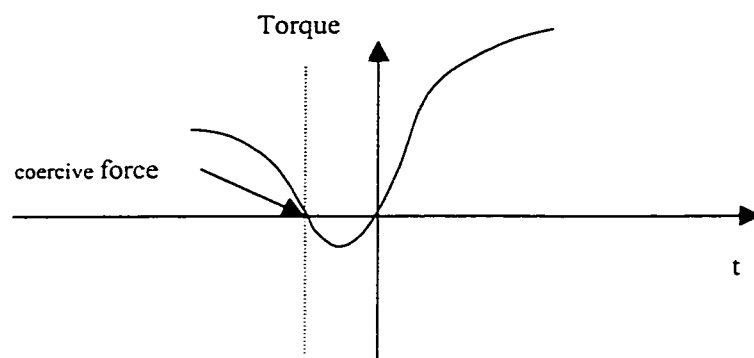
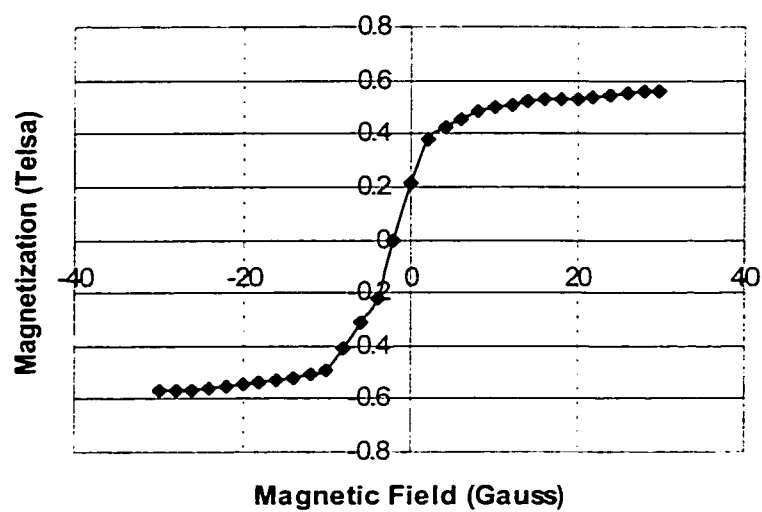
5.2.2 Dynamic Response

The observation of the dynamic response of the device with this actuation mechanism follows the procedures earlier used in the laboratory. In the previous work, a metal lead was routed through a cantilever-in-cantilever structure [11]. With a 10 mA current applied, and by placing the device in an external magnetic field of 0.2 Tesla, the deflection of the cantilever was observed due to the Lorenz force. With this structure, only $\sim 5^\circ$ static deflection was obtained, but the deflection at the resonant frequency of the structure was much larger ($20^\circ - 40^\circ$).

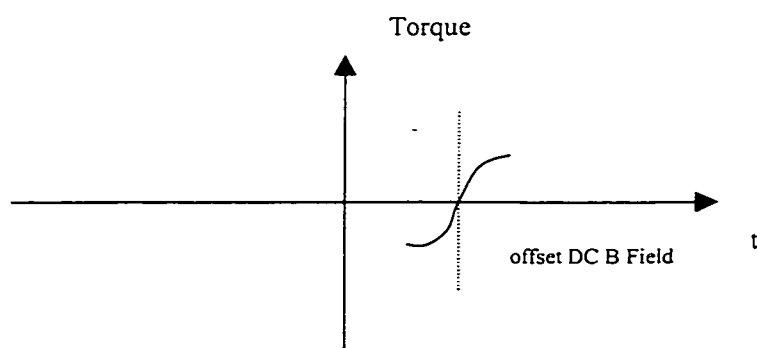
As previously discussed, we have achieved a large static deflection ($\sim 60^\circ$) with an external magnetic field of only 130 Gauss. We expect to obtain a large deflection with low external magnetic field at the resonant frequency of the cantilever structure.

If a device is placed in a magnetic field \vec{B} , a torque \vec{T} will be produced, where $\vec{T} = \vec{M} \times \vec{B}$. If \vec{B} is a sinusoidal magnetic field, the torque produced will have a sinusoidal component as well. If the frequency of the torque is one of the resonant frequencies of the cantilever structure, the mirror should exhibit large deflections even at low magnetic field.

With this in mind, we firstly applied a sinusoidal magnetic field to actuate the device, but little deflection was observed even at the lowest resonant frequency. By further analyzing the hysteresis curve (Figure 3.8) of the Permalloy, we found that, in this case, in the positive portion of the hysteresis curve, both B and M are positive (Figure 5.6a), the torque is positive; in the portion of the Permalloy being magnetized in the opposite direction, both B and M are negative, and so the torque remains positive. The torque only changes sign during the portion from coercive force to zero, in which B changes to negative, but M remains positive. The torque is sketched versus a field of time in Figure 5.6a for this case.



(a)



(b)

Figure 5.6 A sketch of the torque versus time t

To solve this problem, the applied magnetic field was changed so that a DC offset magnetic field was superimposed on the AC magnetic field. The torque produced can now be expressed as

$$\vec{T} = \vec{M} \times \vec{B} = \vec{M} \vec{B}_0 + \vec{M} \vec{B}_1 \sin \omega t \quad (5.2)$$

in which B_0 is a constant magnetic field, B_1 is the magnitude of sinusoidal magnetic field and ω is the frequency of sinusoidal magnetic field.

The first term of (5.2) is an offset component that bends the cantilever to an initial position, while the second term contributes to the resonance of the cantilever structure. The key step is the choice of the DC offset magnetic field. The DC magnetic field should be large enough to magnetize the Permalloy to its saturation during the operation range so that \vec{M} is constant and achieves a maximum torque (Figure 5.6b); however too large DC offset would result in a large initial bending of the cantilever, then smaller bending upwards than downwards at resonance. In our experiment, we chose the DC offset magnetic field of 16 Gauss, which made a $\sim 10^\circ$ initial deflection (see Figure 5.5).

The dynamic deflection of the mirror was measured by the set-up shown in Figure 5.7. The set-up consisted of a He-Ne laser, and a circular screen. The device was glued on the electromagnet and placed at the center of curvature of the screen.

The laser beam emitted by the He-Ne laser was focused on the movable mirror, and reflected to the screen. When the mirror structure deflects, the reflected laser beam spot on the screen moves. Because laser beam spot is quite large, comparable to the area of the micro mirror, the reflected laser beam spot on the screen is not a point, but a relatively large diffuse area. We took the center of the reflected laser beam spot as the origin. When the frequency of the magnetic field is 10 Hz or higher, the platform moves too fast, resulting in a visual expansion of the light spot on the screen into a strip of light. We took the distance between the origin and the edge of the light strip as the distance traveled by the

reflected light beam (D). By measuring D, the angle through which the micro-mirror deflects from can be calculated according to (5.3)

$$\theta = \frac{D}{r} \times \frac{180^\circ}{\pi} \quad (5.3)$$

where θ is the deflection angle of the micro-mirror, D is the distance traveled by the reflected laser beam on the screen, and r is the radius of the screen.

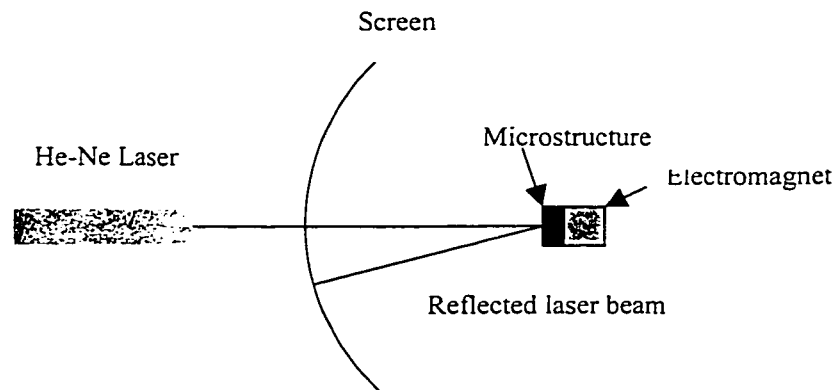


Figure 5.7 The set-up used for dynamic response measurement

By varying the frequency of the voltage applied to the electromagnet from 10 Hz to 2 kHz, We measured two large expansions of the reflected laser beam at frequencies of 380 Hz and 590 Hz. These two frequencies correspond to the first two resonant modes of the structure. Figure 5.8 plots the relative deflection angle of the micro-mirror versus frequency with 0.6 V DC voltage superimposed on a 2 V peak-to-peak sinusoidal signal applied to the electromagnet.

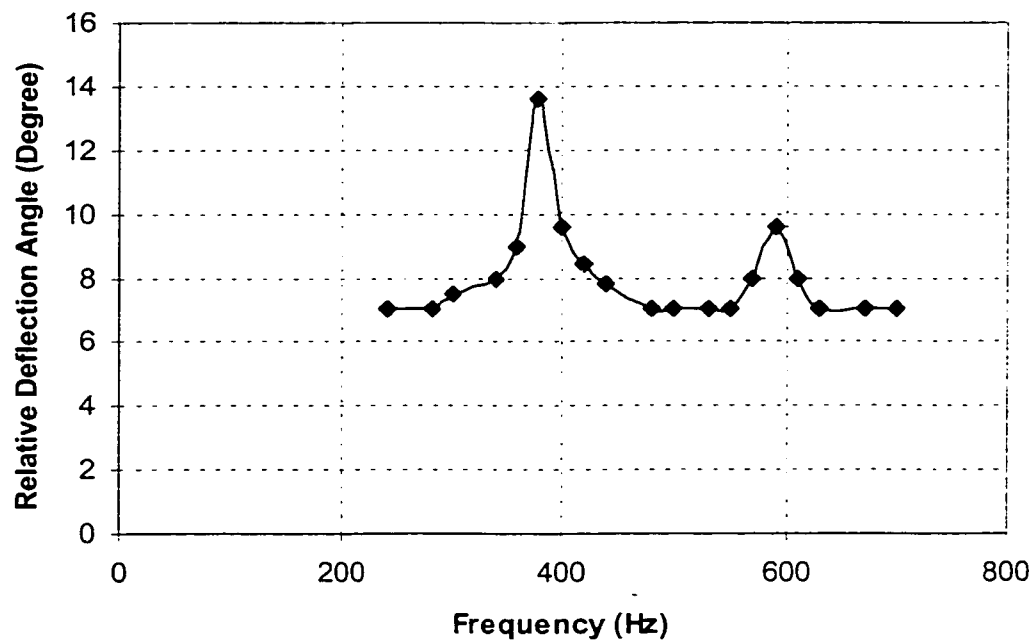


Figure 5.8 Relative Deflection Angle versus Frequency with a 0.6 V DC offset superimposed on a 2 V peak-to-peak sinusoidal voltage applied to the electromagnet

In Figure 5.3, we measured a rapid decrease in amplitude of the magnetic field with frequency increase due to the frequency response of the DC electromagnet. Therefore, Figure 5.8 does not reflect the deflection of the structure under a fixed magnitude of AC magnetic field. We assume that the deflection of the micro-mirror is proportional to the external magnetic field. By rescaling the magnetic field vertically in the ratio of $B(\omega_0)/B(\omega)$, in which ω_0 is the frequency we start measuring, and multiplying the ratios by the deflections at each frequency, we re-plot the deflection versus frequency curve in Figure 5.9. The magnetic field is calculated as 3.6 Gauss AC magnetic field with 2 Gauss offset.

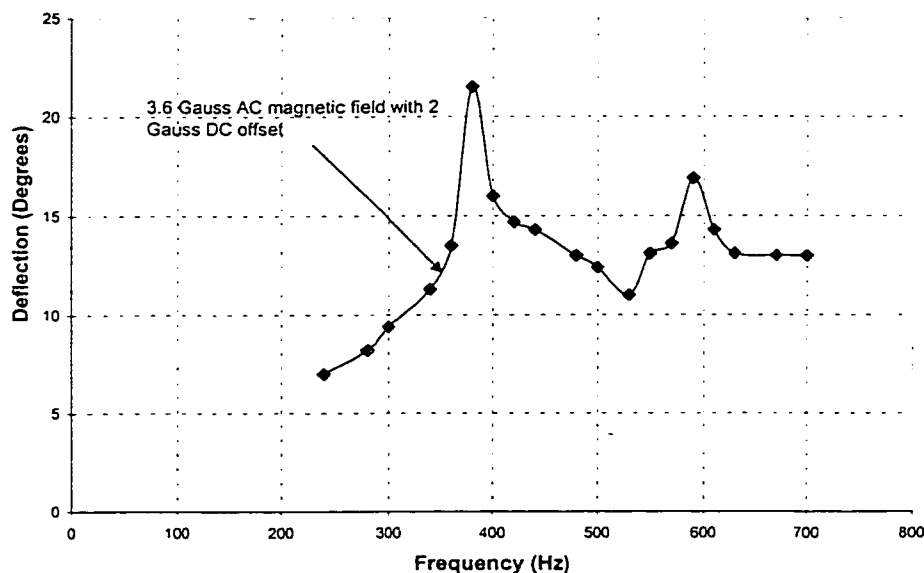


Figure 5.9 Relative deflection angle of the device at 3.6 Gauss AC magnetic field and 2 Gauss offset

We did not observe the third resonant mode predicted by ANSYS. This is probably because the magnetic field generated by the DC electromagnet is too small at this frequency. Even for the first two resonant modes, we measured 15.8% difference at the first mode and 5.3% difference at the second mode. Reasons could be:

1. In ANSYS, the size of the structure we used is the size we designed, but the actual size of the device would be slightly different due to etching (such as left over of etching residue, or undercut of the structure).
2. Mechanical characteristics of the structure we used in ANSYS are for bulk material; they might be different from the thin film material, which constructed our structure.
3. Actual geometry of the Permalloy might be slightly changed during anisotropic etching.

In Figure 5.9, the DC offset magnetic field is only 2 Gauss, while the AC magnetic field is 3.6 Gauss. Although the torque with this offset changes the sign in each half cycle, the Permalloy is not completely magnetized; thus its magnetization \mathbf{M} varies throughout the entire operation cycle. If we change the DC offset to 16 Gauss, which completely magnetizes the Permalloy to its saturation value during the operation range, a much larger deflection was obtained, Figure 5.11 plots the comparison of the deflection of 16 Gauss and 2 Gauss DC offset with same AC magnetic field (3.6 Gauss). From this curve, we can see a large deflection difference ($\sim 30^\circ$) for the same AC magnetic field at resonance.

If the Permalloy is completely magnetized, the deflection angle at resonance will be determined by the magnitude of the AC magnetic field. Figure 5.11 gives the comparison of the deflection angle versus magnetic field of the same DC magnetic field (16 Gauss) offset but different AC component. From this curve, we observed that increasing the AC component increases the deflection at

resonance. Since the AC component is very small compared to the DC component, at frequencies off resonance, the deflections are very close each other.

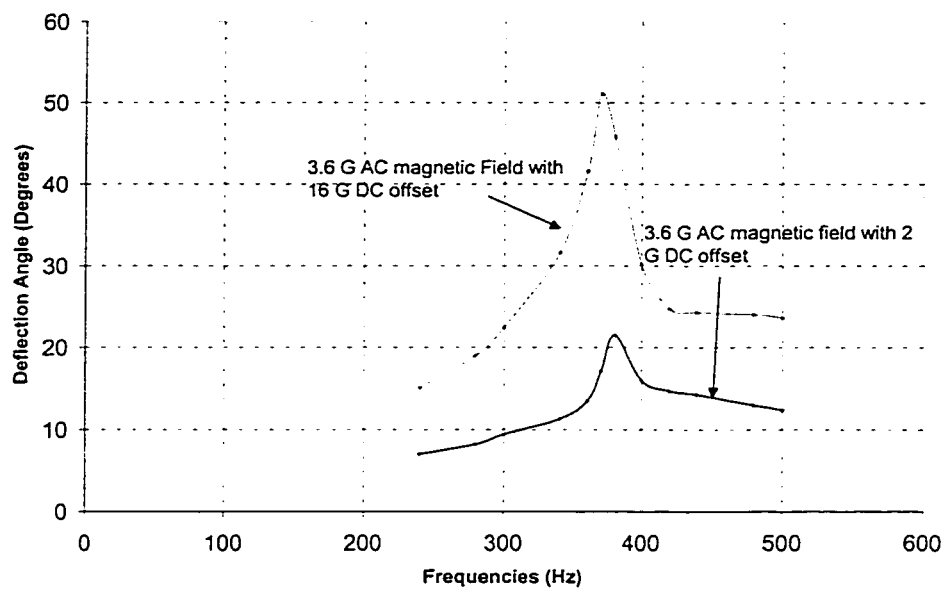


Figure 5.11 Comparison of the relative deflection angles at 16 Gauss and 2 Gauss DC magnetic field with 3.6 Gauss AC magnetic field

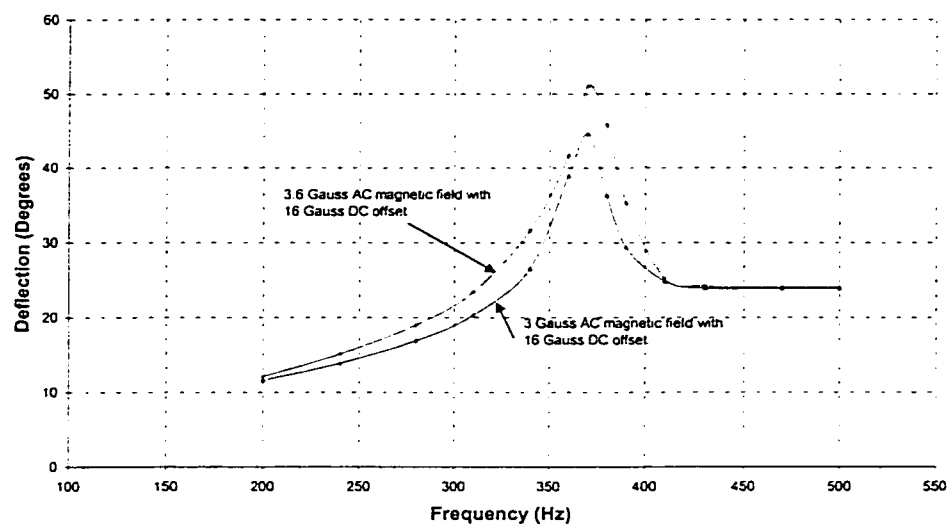


Figure 5.12 Comparison of deflection angle of 3.6 Gauss and 3 Gauss AC magnetic field with 16 Gauss DC offset

Chapter 6

Conclusions and Outlook

The research discussed in this thesis had three objectives. The first objective was to integrate magnetic materials into micromachined devices. The second objective was to introduce a new actuation technique that utilizes the interaction between on-chip Permalloy and an external magnetic field and to develop a theoretical model to predict mechanical response of the microstructure. The third objective was to achieve very large out-of-plane deflection. All of three objectives have been accomplished successfully.

The electroplating process has been demonstrated to be compatible with commercial semiconductor process. With this technique, the thickness of the Permalloy can easily reach 5 μm or more if necessary, to secure a large enough torque to actuate the devices with relatively large size.

A large out-of-plane deflection in weak external magnetic fields has been measured in both the static and dynamic cases. In the static measurement, the platform has been deflected over 60° with an external magnetic field of 130 Gauss. In the dynamic measurement, two resonant frequencies have been measured at 370 Hz and 590 Hz; the deflection angle at 370 Hz is about 45° with a 3 Gauss AC magnetic field superimposed on a 16 Gauss DC magnetic field. This shows that this actuation mechanism is very suitable for applications requiring large deflections.

Efforts have been made to expand this actuation mechanism to a standard CMOS-processed micromachined device. Although this work is not complete and requires further investigation, it provides an alternative or supplement for standard CMOS-processed device actuation using Lorentz force.

Although there are many research activities going on for the development of microstructures with this actuation mechanism, most of them only involve static response of the microstructure; very little progress has been made to investigate dynamic response of the devices.

Some improvements can be made in future potential applications:

1. The magnetic field source can be integrated on the same chip to reduce the physical size of the whole system. The on-chip magnetic field can be generated by applying a current through a metal coil that is fabricated surrounding the structure.
2. Depositing thicker magnetic material to increase the volume of the Permalloy and thus the magnetic torque. The maximum thickness of the Permalloy is, however, limited by some factors. Firstly, increasing the volume of the Permalloy results in the increase of the mass of the movable structures; this will degrade the dynamic response of the devices. Secondly, increasing the thickness of the magnetic material will permit the magnetization to more easily rotate away from its easy axis. Once the magnetization changes direction, the microactuator will abruptly relax to a new equilibrium position with a smaller angle of mechanical deflection and a smaller equilibrium torque.
3. Using LIGA technology, the magnetic material can be deposited with the thickness comparable to the planar size. By pre-magnetizing the

material in the vertical or lateral direction, the remnant vertical or lateral magnetization might be directly used to produce a magnetic field.

4. With multi magnetic fields, both in-plane and out-of-plane can be achieved by switching the direction of the magnetic field. Even 3-D movement could be achieved by superimposing one magnetic field on the other with different direction.
5. Choosing more flexible material such as polysilicon instead of stiff SiO_2 as structural material can increase deflection.
6. By embedding piezoresistors in the structure, the deflection of the structure can be directly measured.

It should be noted that the applications mentioned above are only several preliminary predictions. This is by no means a complete list for the applications of this actuation mechanism. On the other hand, the feasibility for some of the applications listed here needs further investigation.

Bibliography

- [1] S.Bouwster, P. Kemna and R. Legtenberg, "Thermally Excited Resonating Membrane Mass Flow Sensor", *Sensors and Actuators*, 20 (1989) 213-225.
- [2] D.Moser, O.Brand and H. Balters, "A CMOS Compatible Thermally Excited Silicon Oxide Beam Resonator with Aluminum Mirror", *Tech, Digest, Transducers '91*, IEEE, New York, 1991, 547-550.
- [3] T.S.J.Lammerink, M.Elwenspoek, R.H.van Ouwerkerk, S. Bouwstra and J.H.J.Fluitman, "Performance of Thermally Excited Resonators", *Sensors and Actuators*, Vol. A21-A23, 1990, 352-356.
- [4] O.Brand, H.Baltes and U.Baldenweg, "Thermally Excited Silicon Oxide Beam and Bridge Resonators in CMOS Technology", *IEEE, Trans. on Electron Devices*, Vol. 40, No. 10, 1993
- [5] F.R.Blom, D.J.Yntema, F.C.M. van de Pol, M.Elwenspoek and TH. J. A. Popma, "Thin-film ZnO as Micromechanical Actuator at Low Frequencies", *Sensors and Actuators*, A21-A23 (1990) 226-228
- [6] C.J. van Mullem, F.R.Blom, J.H.J.Fluitman and M.Elwenspoek, "Piezoelectrically Driven Silicon Beam Force Sensor", *Sensors and Actuators A*, 25-27 (1991) 379-383
- [7] M. Fischer, H. Graef, and W. Von Munch, "Electrostatically deflectable polysilicon torsional mirror", *Sensors and Actuators A44*, (1994) 83-89
- [8] S. Egawa, T. Niino, and T. Higuchi, "Film actuators: planar electrostatic surface drive actuators" *IEEE Micro Electro Mechanical System (MEMS) Proc.*, pp. 9-14, 1991
- [9] W. C. Tang, T-C. H. Nguyen, and R. T. Howe, "Laterally Driven Polysilicon Resonant Microstructures", *Sensors and Actuators*, vol. 20, no. 1-2, pp. 25-32, 1992

- [10] M. A. Gretillat, P. Thibaud, N. F. De Rooij, and C. Linder “Electrostatic Polosilicon Microrelays Integrated with MOSFETs”, Proc., of the IEEE Micro Electro Mechanical Systems Workshop, Olso, Japan, January, 1994
- [11] B. Shen, “CMOS Actuators”, PHD Thesis, University of Alberta, Canada, 1996
- [12] B.Shen, W.Allegretto, M.Hu, and A. M. Robinson, “CMOS Micromachined Cantilever-in-Cantilever Devices with Magnetic Actuation”, IEEE Electron Dev. Lett., vol. 17, no. 7, pp.372-374, 1996
- [13] B. Shen, W.Allegretto, Y. Ma, M. Hu, and A. M. Robinson, “Cantilever Micromachined Structures in CMOS Technology with Magnetic Actuation”, Sensors and Materials, vol. 9, no. 6, pp347-362, 1997
- [14] B. Wagner and W. Benecke, “Microfabricated actuator with moving permanent magnet”, IEEE Micro Electro Mechanical System (MEMS) Proc., pp. 27-31, 1991
- [15] F.Cardot, J.Gobet, M.Bogdanski, and F. Rudolf, “ Fabrication of a Magnetic Transducer Composed of a High Density Array of Micro-electromagnets with On-Chip Electronics”, Sensors and Actuators A, 43(1994) pp.11-16
- [16] B.Wagner, M. Kreutzer, and W.Benecke, “ Permanent Magnet Micro motors on Silicon Substrates”, Journal of Micromechanical Systems, Vol.2, No.1, March 1993
- [17] J. W. Judy, R. S. Muller, “Magnetically Actuated, Addressable Microstructures”, J. MEMS, vol. 6, no. 3, pp. 249-255, 1997
- [18] S. Liao, “Electrodeposition of magnetic materials for thin-film heads”, IEEE Transactions on Magnetics, vol. 26, no.1, pp.328-332, 1990
- [19] R. A. Miller, G. W. Burr, Y. C. Tai and D. Psaltis, “Electromagnetic MEMS Scanning Mirror for Holographic Data Storage”, Solid State Sensors and Actuators workshop, Hilton Head, SC, June 2-6, 1996
- [20] S. Chikazumi, Physics of Magnetism, New York: Wiley and Sons, Inc..1964

- [21] B. D. Cullity, Introduction to Magnetic Materials. Reading, Massachusetts: Addison Wesley, pp.211, 234, 526, and 527. 1972
- [22] J. W. Judy, "Magnetic Microactuators with Polysilicon Flexures", Master Thesis, Department of Electrical Engineering and Computer Sciences, University of California, Berkeley, 1994
- [23] J. A. Osborn, "Demagnetizing Factors of the General Ellipsoid", Phys. Rev., Vol.67, no.11&12, pp351-357, 1945
- [24] C. H. Ahn, Y. J. Jim, and M G. Allen, "A planar variable reluctant magnetic micromotor with fully integrated stator and wrapped coils", IEEE Micro Electro Mechanical Systems (MEMS) Proc., pp. 1-6, 1993
- [25] C.H.Ahn and M.G.Allen, " A New Toroidal-Meander Type Integrated Inductor with a Multilevel Magnetic Core", IEEE Transactions on Magnetics, Vol. 30, No.1, January 1994
- [26] R.Bozorth, Ferromagnetism. New York: D.Van Nostrand Company Inc., 1951
- [27] U.S. patent, "Electroplating of NiFe Alloy", 1970
- [28] S. P. Timoshenko and J. N. Goodier, Theory of Elasticity, 3rd edition. New York: McGraw-Hill, 1970
- [29] E. P. Popov, Engineering Mechanics of Solids, Englewood Cliffs, New Jersey, Prentice Hall, 1990
- [30] R. J. Roark, in Roark's Formulas for Stress and Strain, W. C. Young, Ed., 6th edition. New York: McGraw-Hill, 1989